A THEORETICAL STUDY OF ANOMERIC METHYL GLYCOSIDES

SEPARATED BY ION MOBILITY SPECTROMETRY: THE SODIUM

ADDUCTS OF ALPHA- AND BETA-METHYL-D-

MANNOPYRANOSIDE

By

PATRICK A. PASTOR

A thesis submitted in partial fulfillment of the requirements for the degree of
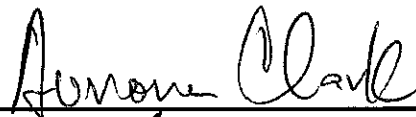
MASTER OF SCIENCES IN CHEMISTRY

WASHINGTON STATE UNIVERSITY
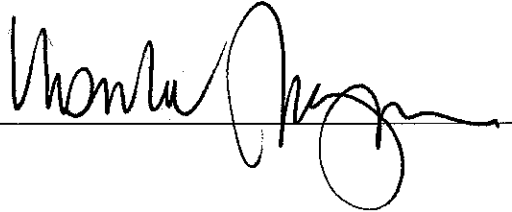Department of Chemistry

August 2007

To the Faculty of Washington State University:

The members of the Committee appointed to examine the thesis of

PATRICK A. PASTOR find it satisfactory and recommend that it be accepted.

_____

Chair

_____

_____

_____

ACKNOWLEDGEMENTS

TABLE OF CONTENTS

A THEORETICAL STUDY OF ANOMERIC METHYL GLYCOSIDES SEPARATED

BY ION MOBILITY SPECTROMETRY: THE SODIUM ADDUCTS OF ALPHA-

AND BETA-METHYL-D-MANNOPYRANOSIDE

Abstract

By Patrick A. Pastor, M.S.
Washington State University
August 2007

Chair: Aurora E. Clark

This investigation is a continuation of previous experimental work on the use of

electrospray ionization/atmospheric pressure IMS for the separation of anomeric methyl

glycosides as metal ion adducts. The separation of methyl-D-mannopyranoside anomers

as Na^+ adducts was found to be profoundly influenced by the polarizability of the drift

gas employed. Density functional theory (DFT) studies were carried out to obtain

theoretical structures for both α- and β-[methyl-D-mannopyranoside]Na^+, which were

characterized in terms of ring conformation, sodium-oxygen bonding, and intramolecular

hydrogen bonding. Neutral methyl-D-mannopyranoside structures obtained by molecular

dynamics simulations followed by further optimization using DFT methods were

compared to the sodiated structures to determine the degree of conformational change

imparted by cation adduction. Using the zero-polarizability approximation, radii were

obtained from experimental results for comparison to radii of gyration calculated for the

theoretical structures of the anomeric sodium adducts.In a preliminary effort to

understand the effect of drift-gas polarizability on the separation of the two anomeric

complexes, dipoles were calculated for the theoretical structures. Differences in size or dipole moment between the α- and β- anomeric sodium adducts were found to be insufficient in accounting for experimentally-obtained collisional cross-sections or drift times, and thus the ion-drift gas interactions involved in separation of the two species.

LIST OF FIGURES

LIST OF TABLES

CHAPTER 1

INTRODUCTION

The application of mass spectrometry to the study of carbohydrate structure is complicated by the technique's inability to unambiguously distinguish isomeric mono-saccharides; the analysis of a mixture of isomers thus necessitates a separation step prior to mass analysis. High-resolution ion mobility spectrometry (IMS) studies of carbo-hydrates are reviewed to demonstrate the technique's utility as a rapid gas-phase separation tool for carbohydrate isomers; particular emphasis is placed on recent studies comparing the effects of different adducting ions and IMS drift gases on carbohydrate isomer separations.

I. Background: Separation of Carbohydrate Isomers Prior to MS Analysis

Glycoconjugates (oligosaccharides attached to cellular lipids and proteins) play a significant role in a number of biological phenomena, including cell-cell recognition and adhesion, receptor binding, signaling, cell differentiation, and immune response (Taylor and Drickamer 2006). The biological functions of glycoconjugates depend on the structure of the carbohydrate moiety (glycan), thus an understanding of glycoconjugate behavior requires explicit knowledge of glycan structure. Elucidating the structure of oligosaccharides within glycoconjugates is a difficult task owing to the presence of monosaccharides (the building blocks of all carbohydrates) which may be in different stereoisomeric forms and vary in linkage and branch positions as well as the anomeric configurations of their glycosidic bonds.

Various methods are used for identification and structural assignment of oligosaccharides, including nuclear magnetic resonance (NMR) (Duus et al 2000) and mass spectrometry (MS) (Zaia 1998, Dell and Morris 2001). While NMR spectroscopy can provide detailed information about stereoisomeric and linkage configurations, it requires much greater sample sizes than mass spectrometry, which, in addition to greater sensitivity, has the ability to separate glycan fragments of different m/z values from a

mixture. The application of mass spectrometry to the study of oligosaccharides dates back more than four decades to the use of permethylation followed by GC-MS for linkage analysis (Bjorndal et al 1967). However, with the advent of "soft" ionization techniques such as fast atom bombardment (FAB), matrix-assisted laser desorption ionization (MALDI), and electrospray ionization (ESI) that allow the investigation of underivatized oligosaccharides, mass spectrometry has found increasing use as a method for structural study of oligosaccharides (Zaia 1998).

The existence of multiple isomers of monosaccharides complicates the determination of oligosaccharide sequence and structure by mass spectrometry. For instance, the 16 D- and L- aldohexoses can exist in 2 anomeric configurations (Figure 1.1) and 2 pyran/furan isomers within an oligosaccharide, giving a total of 64 configurations with the same m/z. These stereoisomers frequently dissociate to yield roughly identical mass spectra, so that one cannot establish the stereochemistry of monosaccharides from fragmentation patterns, let alone the structure of their parent molecule. Owing to the "stereochemical blindness" of mass spectrometry, product ions must be separated based upon physical properties other than m/z prior to mass analysis. This is typically achieved using traditional chromatographic techniques, including high-performance liquid chromatography (HPLC) (Imanari et al 1996), gas chromatography (GC) (Bjorndal et al 1967), and capillary electrophoresis (CE) (Honda 1996).

Due to the low volatility of carbohydrates, gas chromatographic separation requires extensive derivatization. Liquid chromatographic methods pose problems due to the narrow ranges of polarities and size of many sugar isomers, which mean that the differential partition coefficients upon which these methods rely may not be sufficient for differentiating isomeric carbohydrates. In addition, the lack of electrical charge and

hydrophilic nature of carbohydrate molecules mean that LC and CE separation conditions may be difficult to couple to mass spectrometric detection (Gabryelski and Froese 2003a).
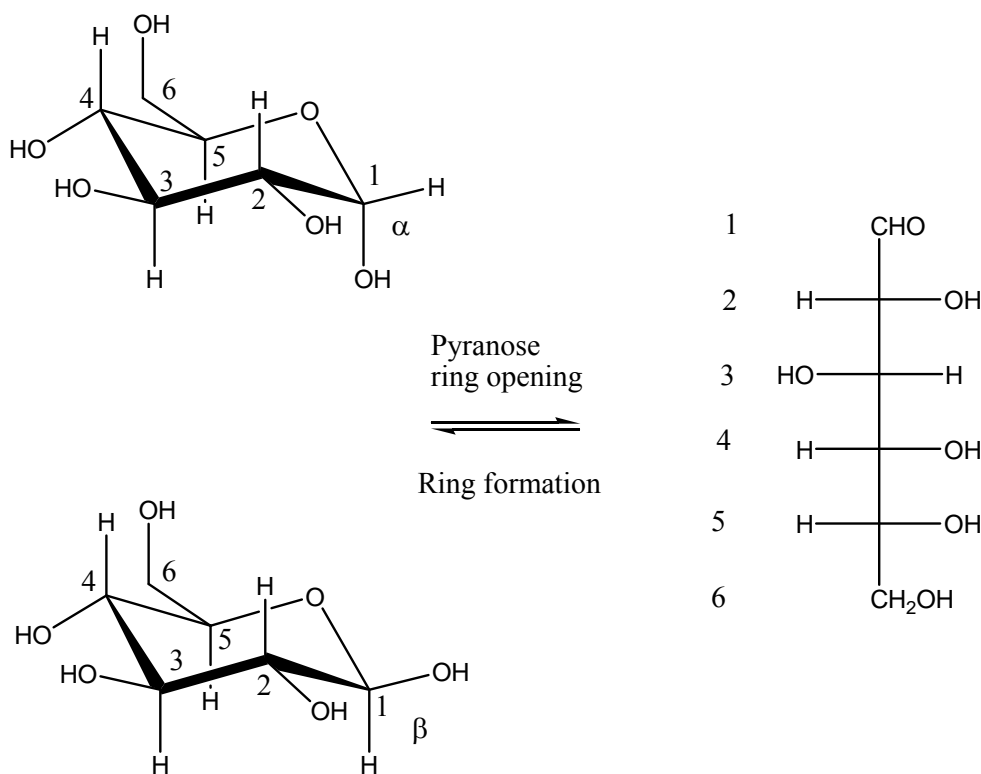
Figure 1.1 The two anomeric ring forms of D-glucopyranose. Anomers differ in configuration at C1 (known as the anomeric carbon). In the α configuration, the C1 hydroxyl group is axial; in the β configuration, it is equatorial. (The open-chain form of glucose is shown in a Fischer projection).

In recent years, ion mobility spectrometry (IMS), a technique which separates gas-phase ions based on their size as expressed through differences in their mobilities in a buffer gas, has been proposed as a rapid gas-phase separation technique for isomeric carbohydrates. The resolving power of IMS is superior to that of liquid chromatographic methods and similar to that of gas chromatography. As a gas-phase separation method, the separation time during an IMS experiment is in the millisecond range, allowing for reduced analysis time and improved sample throughput relative to liquid-phase methods. The application of IMS to the separation of isomers has been demonstrated almost since

the technique's inception in the early 1970s; Karasek et al. (1974) and Hagen (1979) used IMS to separate isomeric benzene derivatives. More recently, IMS has been employed in the separation of amino acid (Beegle et al 2001), peptide (Wu et al 2001) and napthenic acid isomers (Gabryelski and Froese 2003b).

On the other hand, only a few studies involving the application of IMS to carbohydrates have been reported, and separation of isomers has been demonstrated in only the most recent of these studies. Using low pressure (2-5 Torr) IMS along with molecular dynamics calculations, Lee et al (1997) studied the gas phase structures of several MALDI-ionized sodiated oligosaccharides including three tetraose isomers and two hexaose isomers. While differences in arrival times were observed between the two groups of sugars, they could not be separated into isomeric forms. Liu et al (1997) also applied low-pressure IMS to the study of oligosaccharides, analyzing the deprotonated ions of melezitose, raffinose, and α-, β-, and γ-cyclodextrins produced by negative electrospray ionization. While unable to resolve raffinose and melezitose to the extent required for separation due to the observed 1.3% difference in mobility (below the 2% required), they concluded that the two existed in different conformations. In addition, the authors were able to distinguish isobaric (m/z 221) CID fragment ions formed by raffinose from those formed by α-cyclodextrin; the two showed a 5.2% difference in mobility values.

Using the fact that IMS resolving power increases with drift-tube pressure, Lee et al (1998), used an atmospheric pressure ion mobility spectrometer with an ESI ion source to detect a variety of carbohydrates (including simple sugars, amino sugars, and sugar alcohols). In this study, reduced ion mobility values were obtained for a series of 21 carbohydrates of varying molecular weights.

While isomeric carbohydrates were not resolved from a mixture, differences in reduced ion mobilities suggested that the resolution of carbohydrate isomers was possible. For example, the stereoisomeric amino sugars D-mannosamine (t_d: 13.54, where t_d is the drift time in ms, defined as the time an ion requires to traverse the drift region of an ion mobility cell), D-galactosamine (t_d: 13.84), and D-glucosamine (t_d: 12.87) were mobility separated. Leavell et al (2002) reported the application of ion mobility spectrometry and density functional theory (DFT) calculations to examine the conformations of covalent diethylenetriamine glycosylamine derivatives of hexoses (all β-anomers) as [Zn(II)/chloride]$^+$ adducts. The cross-sections of the glucose, galactose, and mannose complexes differed sufficiently for separation by IMS. Most significantly, DFT studies showed that the stereochemistry of the monosaccharide dictated the conformation and metal coordination site of the complex.

The first study in which carbohydrate isomers were in fact resolved from a mixture was performed by Gabryelski and Froese (2003a), who used high-field asymmetric waveform ion mobility spectrometry (FAIMS), a method that responds to changes in ion mobility under high-field conditions, to separate anomeric, position, and linkage isomers of disaccharide decanoic acid derivatives. Using a positive ESI source, anomers and position isomers were separated as cesium adducts, and linkage isomers were separated as sodium complexes; in the negative mode, the anomers were best separated as haloacetate complexes and the linkage isomers as chloride complexes or deprotonated ions. Some position isomers were best separated as chloride complexes, others as haloacetate complexes. This demonstrates that in FAIMS, the identity of the adducting ion plays a role in isomeric separation of carbohydrates; raising the possibility that the same may be true for conventional IMS.

Within the Hill group, Clowers et al (2005), demonstrated separation of several disaccharide alditol linkage isomers isolated from O-linked glycoproteins, and three trisaccharide linkage isomers using atmospheric pressure IMS. The species were generated by positive electrospray ionization as carbohydrate-sodium complexes.

Dwivedi et al (2006), using atmospheric pressure IMS, reported the first separation of monosaccharides—the building blocks of all carbohydrate compounds. Simple isomeric mixtures of reducing monosaccharides—the pentoses ribose and xylose, the hexoses glucose and fructose, and the amino sugars glucosamine and mannosamine were ionized using an ESI source. Most reducing species produced multiple peaks corresponding to different anomeric and cyclic forms (Figure 1.2).

In addition, these researchers reported separation of the anomeric isomers of the methyl glycosides of Glc, Gal, and Man. Here, a single peak was observed for each anomer, as intercoversions between anomeric positions and ring conformations (pyranose and furanose) were precluded by the formation of an acetal (Figure 1.3). Separation was defined in terms of a difference in IMS drift times of greater than 0.2 ms between isomers.

II. Effects of Adducting Cation and Drift Gas on IMS Separation of Methyl Glycosides

In light of Gabryelski and Froese's findings that the identity of the adducting cation unpredictably affected the FAIMS separation of different carbohydrate isomers, the effect of the adducting cation on the IMS separation of isomeric methyl glycosides was examined by Dwivedi et al (2006). The anomeric methyl glycosides of Glc, Gal, and Man were studied as adducts of sodium $[M + Na]^+$ (m/z 217) and cobalt acetate $[M + Co(CH_3COO]^+$ (m/z 312). Methyl galactopyranosides were also studied in the presence of

several other cations including Ag^+, Cu^{2+}, Ca^{2+}, Hg^{2+}, and Pb^{2+} as the acetate salt and Co^{2+} and Pb^{2+} as the acetylacetonate salts.
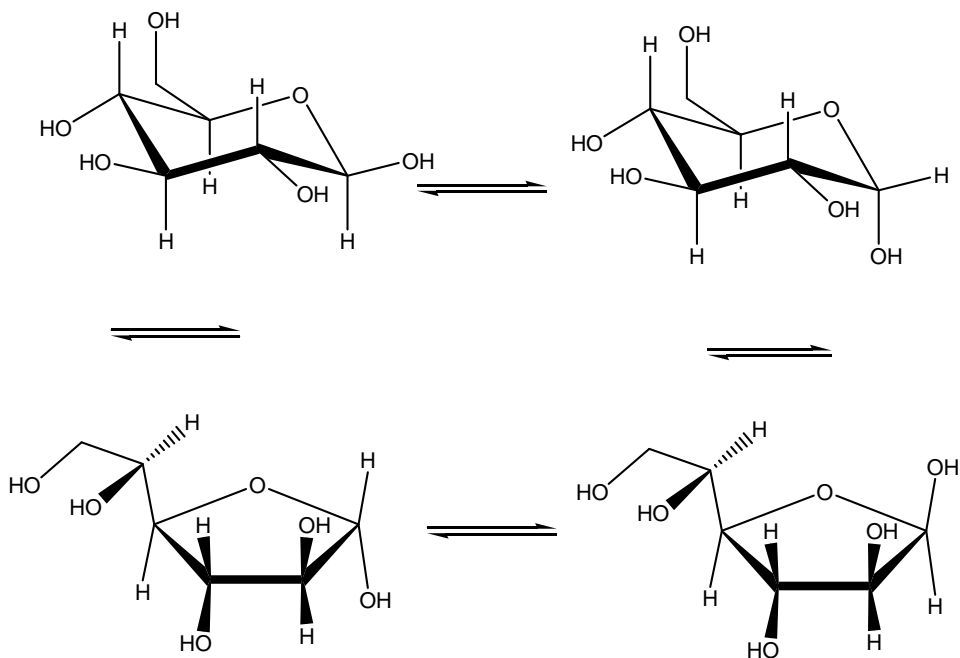
Figure 1.2 Mutarotation: the interconversion of α- and β- anomeric forms, six-member (pyranose) and five-member (furanose) ring forms of D-glucose.

The identity of the cation, as well as the coordination of the counterion in the case of the 2+ cations (all of which formed singly charged complexes) was found to significantly affect the separation factor (as in chromatography, separation factor in IMS is defined as the ratio of a longer drift time to a shorter drift time).

Using nitrogen as the drift gas, as is common practice in high-resolution IMS (Hill et al 2002), the anomers methyl α-D-galactopyranoside (α-MeGal) and methyl-β-D-galactopyranoside (β-MeGal) were resolved as adducts of both sodium and cobalt acetate; resolution was slightly better with sodium as the adducting ion. On the other hand, the sodium adducts of α-MeGlc and β-MeGlc showed only partial separation; a separation well beyond baseline was achieved using cobalt acetate as the adducting ion.

The sodium adducts of α-MeMan and β-MeMan showed no separation, while the cobalt acetate adducts showed only partial separation

Reducing sugar
(hemiacetal)

Methyl glycoside
(acetal)
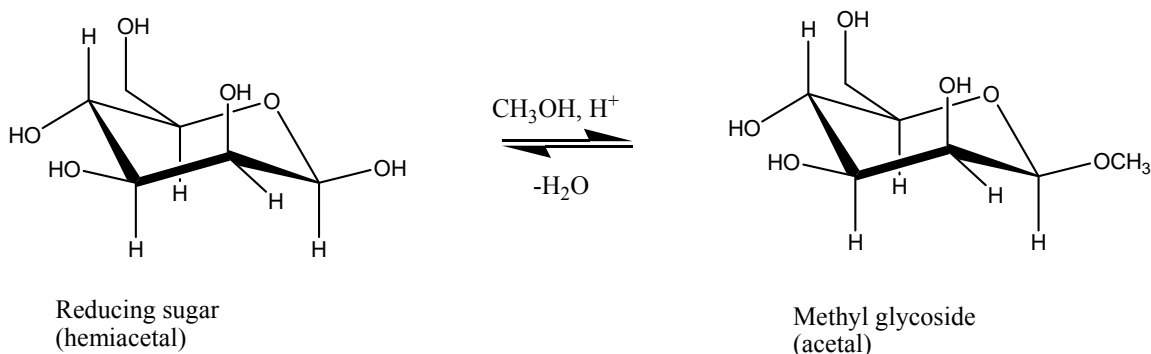
Figure 1.3 β-D-mannopyranose, a reducing monosaccharide (left); methyl- β-D-mannopyranoside (right), a methyl glycoside. Mannose is described as a reducing sugar because it retains an aldehyde functional group, capable of reducing Cu^{2+} and other inorganic ions, in the form of a hemiacetal. In methyl D-mannopyranoside and other methyl glycosides, the hemiacetal group has been converted to an acetal, and the monosaccharide is no longer reducing or capable of mutarotation.

The separation of epimeric methyl glycosides (Figure 1.4) was demonstrated, with baseline resolution of two epimer pairs— α-MeGlc and α-MeMan, epimeric at the C2 position, and β-MeGlc and β-MeGal, epimeric at the C4 position, as sodium adducts in N_2. Importantly, the separation of epimeric pairs, and the differences in separation between different anomeric pairs and between different adducts of the same anomeric pair, indicate that separation is sensitive to both the identity of the adducting ion and the stereochemistry of the monosaccharides.

While nitrogen is among the most frequently used drift gases, variation of drift time with drift gas polarizability has been reported for a variety of analytes, indicating that an increase in drift gas polarizability might increase resolution between isomers (Asbury and Hill 2000a, Beegle et al 2002, Matz et al 2002).
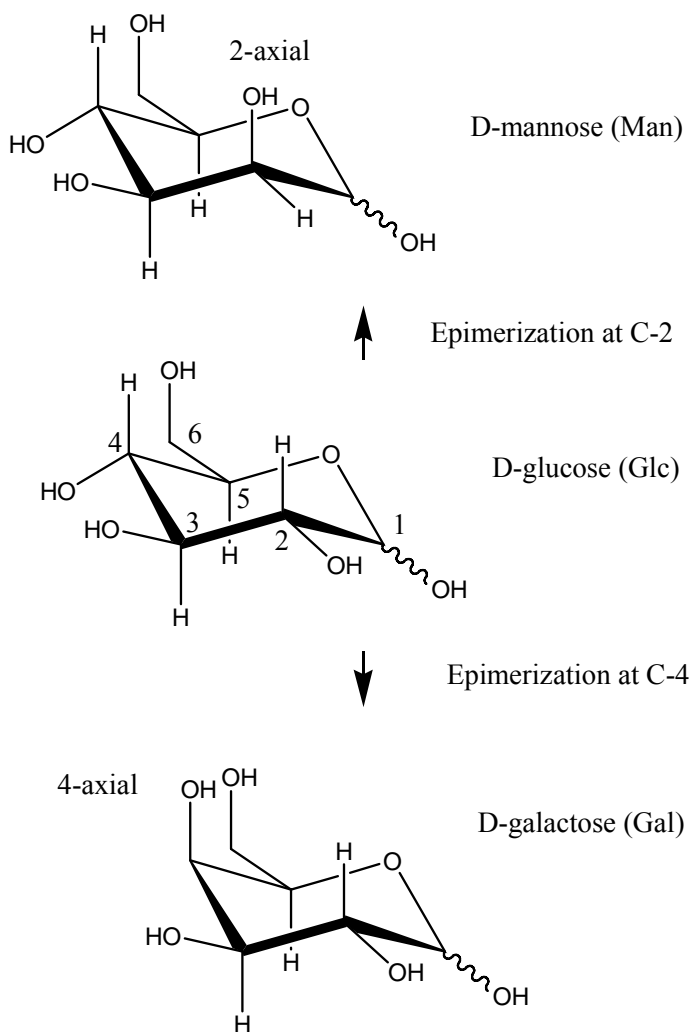
Figure 1.4 Epimers are species that differ in stereochemistry at a single non-anomeric carbon. Glucose (Glc) and mannose (Man) are epimeric at C-2; Glc and galactose (Gal) are epimeric at C-4. (The wavy bond means that the configuration at C-1 is not defined.)

When CO_2 was used in place of N_2, α-MeMan and β-MeMan were baseline separated as sodium adducts; separation factors between anomers improved to a lesser extent for the other sodiated methyl glycosides. In CO_2, a separation factor of 1.03 was observed, with drift times of 20.96 and 20.42 ms for α-MeMan and β-MeMan, respectively. This is in contrast to the experiment conducted in N_2 where the separation factor was 1.01, insufficient for resolving the two isomers (Figure 1.5).
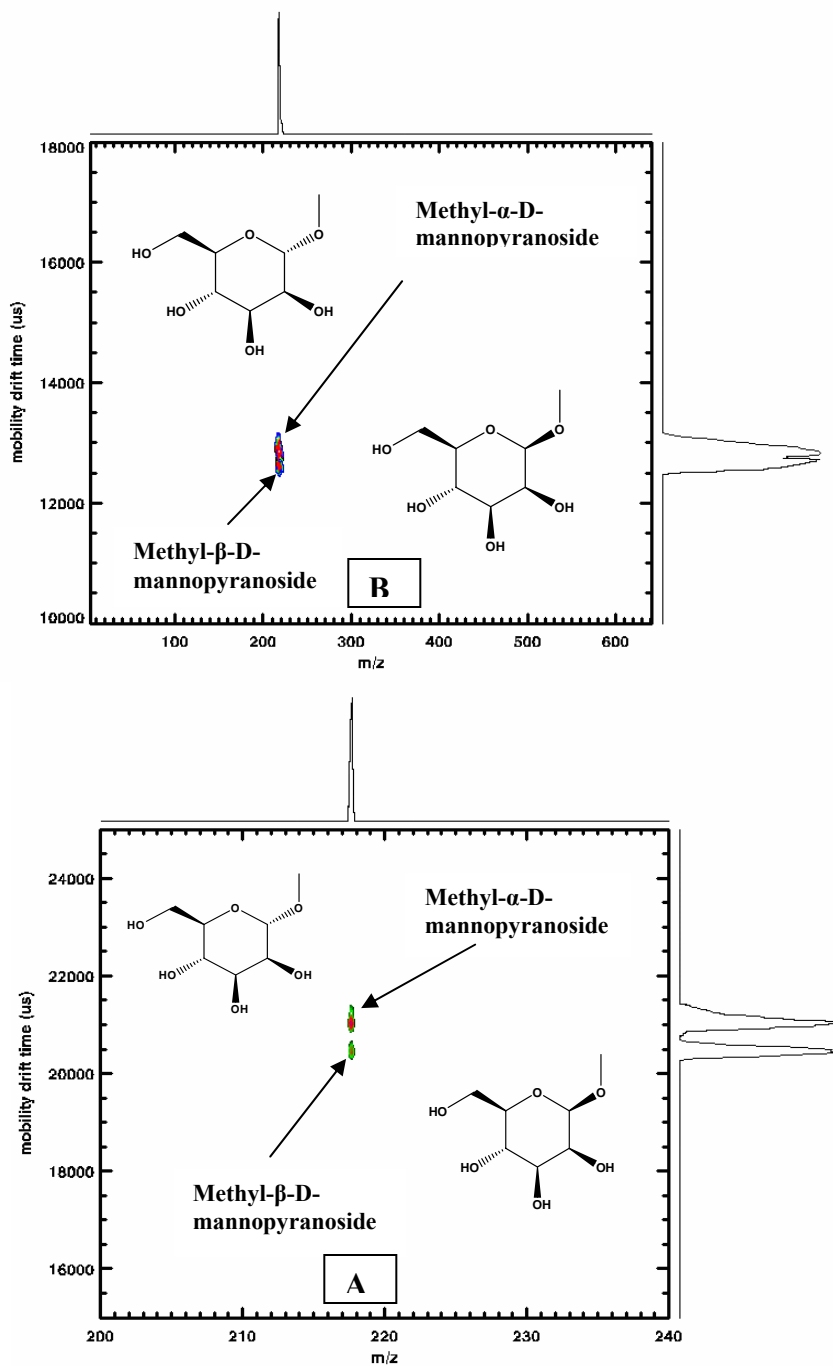
Figure 1.5 IMS-MS spectra of methyl-D-mannopyranoside anomers as sodium adducts (m/z 217) in two different drift gases: CO_2 (A) and N_2 (B). The α- and β- anomers were baseline separated in CO_2 but barely resolved in N_2. These measurements were performed at 514 V/cm and 699 mmHg pressure (Dwivedi et al 2006).

These results indicate that the separation properties of methyl glycoside

monosaccharides can be changed by varying the adducting ion and the drift gas, and are

thus dependent on two factors: a) the degree of conformational change imparted by the adducting cation, and b) the interactions between the adduct and the drift gas.

An understanding of how these two factors influences the separation of isomers can be obtained through theoretical calculations, chiefly geometry optimization using molecular mechanics and electronic structure methods, as in previous literature (Leavell et al 2002, Hill et al 2002). The work presented here examines the interactions of the monosaccharide structure with the adducting cation, and the [MeMan]Na$^+$ adduct's interaction with the drift gas as examined by theoretical calculations and analysis of previously obtained experimental results.

The choice of sodium adducts of anomeric methyl glycosides as the system for this theoretical study was dictated by the fact that sodium adducts are the most abundant ions for each methyl glycoside species, even without the addition of sodium to the solution. The predominance of $[M + Na]^+$ product ions appears to reflect a well-attested phenomenon in positive electrospray studies of carbohydrates (Colas et al 2006). As polar neutral molecules, lacking strongly acidic or basic groups, carbohydrates are likely to be charged by the formation of adducts, and $[M + Na]^+$ adducts form even in the presence of very low concentrations of sodium (Cech and Enke 2001). Given the fact that in electrospray ionization mass spectrometry, carbohydrate ions are found primarily as sodium adducts, the ability to separate isomeric monosaccharides as sodium adducts using ambient pressure IMS could make a significant contribution to carbohydrate sequencing. To further apply this phenomenon to IMS separation of isomeric monosaccharides requires an understanding of the effect of Na$^+$ adduction on monosaccharide conformation, as well as the interactions of the adduct with drift gas molecules.

CHAPTER TWO

EXPERIMENTAL METHODS AND DATA ANALYSIS

Using ESI-APIM-tof-MS measurements of collision cross-sections (Dwivedi et al 2006) for α- and β-methyl-D-mannopyranoside-Na$^+$ made in three drift gases (Ar, N_2, and CO_2), ion radii were estimated using the hard-sphere approximation in each gas so as to determine the zero-polarizability radii of the methyl-hexopyranoside-Na$^+$ adducts for comparison with radii of gyration calculated in CHARMM for theoretical structures.

I. Electrospray Ionization Atmospheric Pressure Ion Mobility Time-of-Flight MS

The configuration of the instrument used in this and previous studies of separation of

methyl glycosides and oligosaccharides (Dwivedi et al 2006, Clowers et al 2005) is one

wherein an ambient pressure high-resolution IMS (APIMS) drift tube is coupled to an

electrospray ionization source and an orthogonal reflector time-of-flight mass

spectrometer (TOFMS), (Steiner et al. 2001).
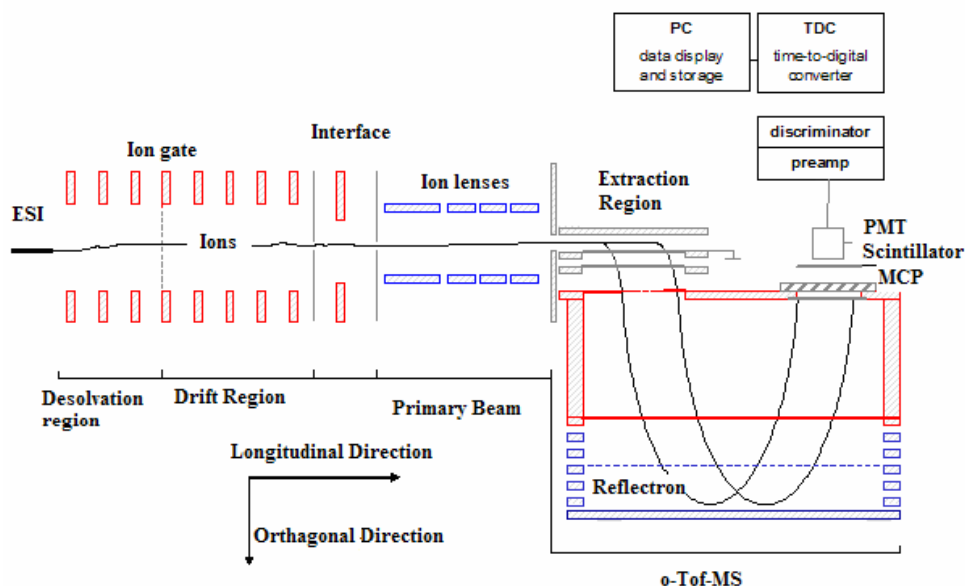
Figure 2.1 Schematic diagram of ESI-APIM-tof-MS device. The atmospheric pressure ion mobility cell is 25 cm in length with a desolvation region of 8.4 cm and a drift region of 18.6 cm. The atmosphere to vacuum interface is a 250 μm pinhole orifice which introduces the ions into the mass spectrometer through a pressure transition region. The ions are then focused via a series of lenses into an orthogonal time-of-flight mass spectrometer (40 cm) with a reflectron providing a total ion path length of 1 m. The APIMS provides an average resolving power of 70 and the mass spectrometer has an average resolution of 1500 (Courtesy of IonWerks, Inc.)

As shown in Figure 1, the basic components of the ESI-APIM-tof-MS device are: 1) ESI ion source; 2) the APIMS drift tube; 3) the pressure interface; 4) the orthogonal reflector TOF m/z analyzer, and 5) the data acquisition system. The APIMS has a stacked-ring design as described by Wu et al. (1998), and is divided into two regions: a desolvation region (8.4 cm in length) and a drift region (18.6 cm in length). Both regions are made up of alternating alumina spacers and stainless steel rings, the latter connected by high-temperature resistors (500 kΩ for the desolvation region and 1 MΩ for the drift region). The two regions are separated by a Bradbury-Nielsen ion gate.
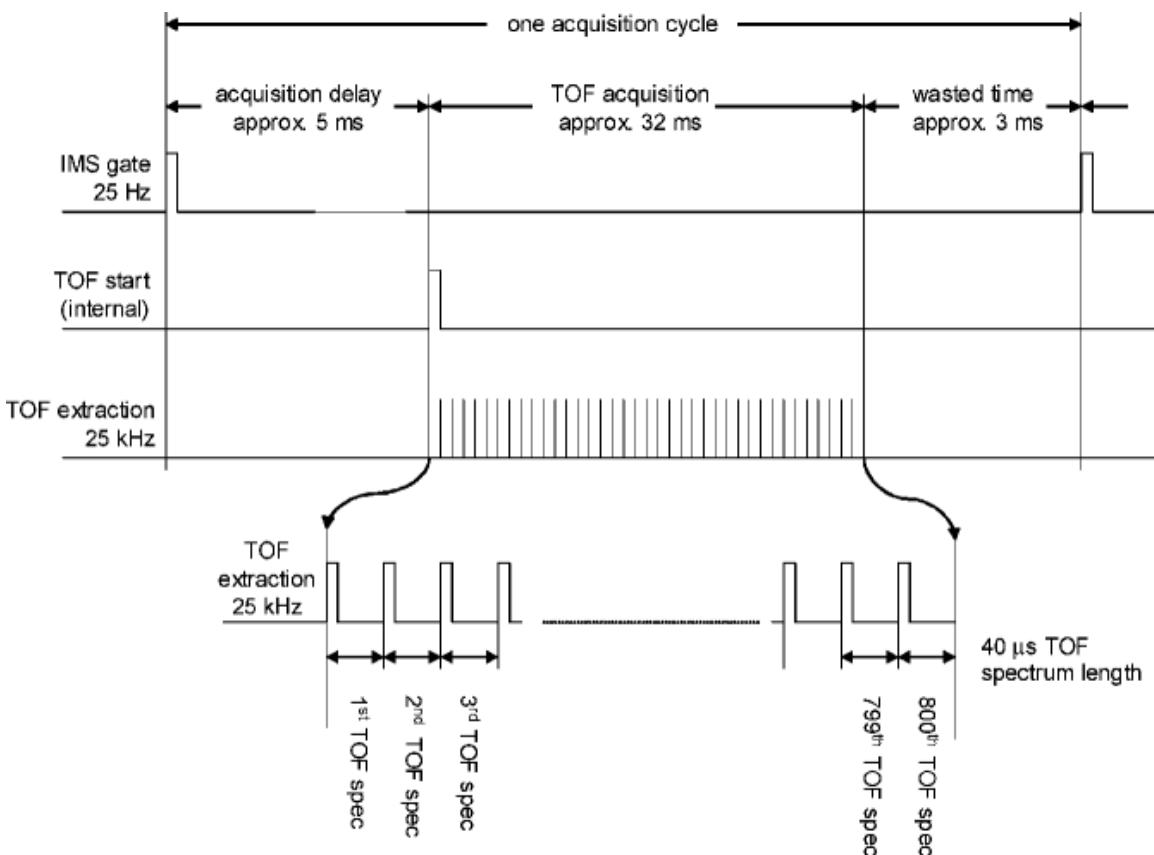
Figure 2.2: Typical APIM-tof-MS acquisition timing sequence. Ions are gated into the drift region for 200 μs at a frequency of 25 Hz, providing 40 ms for each IMS mobility spectrum. Allowing for a 5 ms acquisition delay, the APIMS is sampled every 40 μs, providing sampling of each mobility spectrum with 800 nested TOFMS spectra extracted (Steiner et al 2001).

The orthogonal TOFMS (ORTOF), described in detail by Fuhrer et al (2000) and Steiner et al. (2001) serves as a mass analyzer, allowing collection of both mass spectra

and mobility data. Time-of-flight analyzers have a significant advantage over other mass spectrometers for IMS-MS; unlike quadrupole mass spectrometers, they can acquire all ions simultaneously without the need for sequential scanning of m/z values. The key advantage of coupling IMS with TOFMS is the two-dimensional data matrix of simultaneous drift times and flight times (Figure 2). The time scale of the drift times (ms) is three orders of magnitude greater than that of the flight times (µs).

II. Mobility Constants, Resolving Power, Separation Factor, and Experimentally Determined Cross Sections

A. Mobility and Cross Section. The mobility constant K (cm^2 V^{-1} s^{-1}) of an ion moving through an inert gas at constant temperature and pressure is defined by Equation 2.1

$$K = \frac{v_d}{E} = \frac{L^2}{V t_d} \tag{2.1}$$

where v_d is the average drift velocity (measured in cm s^{-1}), E (V cm^{-1}) is the electric field (assuming low-field conditions) , t_d is time (s) required for an ion to traverse the length L (cm) of the IMS drift tube (the distance from the ion gate to the detector), and V is defined as the change in voltage across L.

In order to take into account the changing environmental conditions and compare mobility across different experimental systems, the mobility can be defined in terms of a "reduced" mobility constant defined with respect to standard temperature and pressure as

$$K_0 = K \left(\frac{273.15}{T} \right) \left(\frac{P}{760} \right), \tag{2.2}$$

where T is the effective gas temperature (K) and P is the gas pressure (Torr) in the drift tube.

In IMS, separation is achieved due to differences in the collision cross-sections of the ions as they traverse the drift region, where they undergo random collisions with drift gas

molecules and accelerations due to the electric gradient across the length of the tube. The collision cross-sections between the ions and neutral drift gas are defined by interactions between the ion and the drift gas, which depend on the geometry (conformational structure) of the ionic species.

The collision cross-section is inversely proportional to mobility; a more compact ion (with a lower collisional cross-section) has a higher mobility, as it experiences fewer collisions with drift gas molecules and thus travels faster, while an ion with a larger cross-section has a lower mobility. Experimentally, the average ion-neutral collision cross-section (Ω) is measured using (Equation 2.3) of Revercomb and Mason (1975):

$$\Omega = \left[\frac{3}{16N_A}\right]\left[\sqrt{\frac{2\pi}{\mu kT}}\right]\left[\frac{ze}{K}\right], \tag{2.3}$$

where N_A is the number density of the drift gas (molecules/cm^3), μ is defined as the reduced mass [$= mM/(m + M)$] (kg) of an ion of mass m (g mol^{-1}) and the neutral drift gas of mass M (g mol^{-1}), k is Boltzmann's constant (J K^{-1}), z is the number of charges on the ion, e is the unit charge (coulombs), and K is the mobility (cm^2 V^{-1} s^{-1}). Number density N_A is defined as $N_A = P/kT$ where P is atmospheric pressure (atm), k is Boltzmann's constant (L atm K^{-1}) and T is temperature (K).

B. Resolving Power and Separation Factor. The efficiency of separation, or resolving power of IMS, is typically defined as a single-peak quotient: drift time divided by temporal peak width at half height ($w_{1/2}$) (Siems et al, 1994)

$$R_p = \frac{t_d}{w_{1/2}}. \tag{2.4}$$

The resolving power, while it measures separation efficiency, does not indicate the degree to which two peaks are separated. This is defined by the difference in drift times between two peaks (Δt_d) divided by the average baseline peak width (w_{base})

$$R = \frac{\Delta t_d}{w_{base}}. \tag{2.5}$$

Equation (2.5) allows for the use of a new term, the separation factor (α) or selectivity, defined as

$$\alpha = \frac{t_d^2}{t_d^1} = \frac{K_1}{K_2}, \tag{2.6}$$

where K_1 is the mobility of the faster compound and K_2 the mobility of the slower compound.

C. Drift Gas Polarizability: Effect on Resolving Power and Separation Factor

In most IMS studies in which ionic size is determined and compared with that of modeled structures, He has been used as the buffer gas in order to eliminate the effects of polarization and other long-range drift gas contributions from the modeled interaction. However, higher resolving powers, and thus more accurate determinations of ion size, can be obtained with drift gases more polarizable than He, as indicated by Revercomb and Mason's expression for measured peak width in IMS:

$$w_h^2 = t_g^2 + \left[\frac{(16kT)\ln 2}{Vez} \right] t_d^2. \tag{2.7}$$

In equation (2.7), t_g is the original pulse width, k is Boltzmann's constant, T is the temperature (K) of the drift gas, V is the potential across the length of the drift tube, e is the unit charge, z is the number of charges on each ion, and t_d is the drift time. From eq. (2.7), it is clear that a decrease in the peak width, and thus an increase the resolving

power, is obtained by increasing the voltage drop V or reducing the total pulse width t_g (Asbury and Hill 2000b).

It has been shown that for a given instrument and set of operating parameters, drift times increase with drift gas polarizability as the pulse width contribution to the total peak width is reduced. In addition to longer drift times, higher-polarizability drift gases can withstand higher voltages without breakdown. Asbury and Hill (2000a) have further shown that the use of different drift gases can directly change the separation factor α. In this case, ions (peptides and low molecular weight compounds) showed the greatest mobility in helium and the lowest in carbon dioxide, but the percent change in mobility differed for each compound, thus changing the α value.

While drift gas mass influenced the α value when the masses of the drift gas and the ion were of similar magnitude, polarizability made a contribution in nearly all cases. As drift-gas polarizability does not affect all ions equally, changing the drift gas can enable separation, analogous to the chromatographic use of different mobile and stationary phases to change selectivity.

D. Method of Zero-Polarizability Radii

A new method has been developed that uses higher-polarizability drift gases to estimate ion size from IMS measurements (Hill et al 2002). This involves measuring the experimental ionic radii (based on the rigid-sphere model) in three to four drift gases of differing polarizability (Table 2.1). It was found by Asbury and Hill (2000a) and Beegle et al (2002) that in the drift gases Ar, N_2, and CO_2, there is a linear relationship between effective ion radii and drift gas polarizability, a phenomenon which can be accounted for by the relative weakness of long-range ion-dipole interactions between the ion and the

drift gas, which allows the ion-neutral cross section to be accounted for by the geometries

of these species.

Table 2.1. Drift gas mass and polarizability (Asbury and Hill 2000a).

Drift gas	Mass (Da)	Hard-sphere radius[a] (200 °C)	Polarizability (x 10^{-24} cm^3)
argon	40	1.68	1.641
nitrogen	28	1.76	1.740
carbon dioxide	44	2.06	2.911

[a] Hard sphere radii calculated using viscosity data obtained from the *CRC Handbook of Chemistry and Physics*, 87th ed., David R. Lide, editor (2006).

In the method of zero-polarizability radii, the radii of the drift gas molecules are

determined using the hard-sphere model given by

$$r^2_{gas} = \frac{1}{4}\left(\frac{5}{16\pi^{1/2}}\right)\left(\frac{(MRT)^{1/2}}{N_A\eta}\right),$$ (2.8)

where M is the mass of the gas molecule, R is the gas constant, T is the temperature, N_A

is Avogadro's number, and η the gas viscosity. Ion radii are determined using the hard-

sphere collisional cross-section

$$\Omega = \pi\,(r_{ion} + r_{gas})^2.$$ (2.9)

As the polarizability of the drift gas increases, so does the effective radius of the drift gas;

however, this is dependent on both the drift gas and the specific ion. The effective drift

gas radius r_{gas} is a combination of two terms

$$r_{gas} = r_p + r_v,$$ (2.10)

where r_p is the portion of the radius due to the ion-neutral long-range polarization

interaction and r_v is the intrinsic radius of the gas molecule as calculated in Eq. (8).

The effective (experimentally measured) radius, r_{eff}, of the ion can be defined as

$$r_{eff} = r_{ion} + r_p = \sqrt{\frac{\Omega}{\pi}} - r_v. \tag{2.11}$$

The removal of r_p (the contribution of the drift gas) from the measured radius r_{eff} is known as the zero-polarizability method. This method takes advantage of the linear relationship between drift-gas polarizability and effective ion radius demonstrated in previous studies. In this method, it is assumed that the ionic radius itself does not change significantly in the presence of different drift gases, but rather that the apparent drift gas radius (r_{gas}) increases with polarizability. The radius of the ion in a hypothetical zero-polarizability environment ($r_p = 0$) can thus be found as the y-intercept of a plot of effective radius versus polarizability. In the zero-polarizability method, the measured radius is defined as

$$r_{eff} = m\alpha + r_{ion}, \tag{2.12}$$

where m is the slope of the line, α is the polarizability of the drift gas, and there is a linear relationship with r^2 above 0.99. The intrinsic ion radius in a zero-polarizability environment is assumed to be comparable to the average radius of a candidate structure generated through molecular dynamics simulations or density functional theory (DFT) calculations, as both are radii determined in vacuo. The slope (m) of the zero-polarizability equation is also significant, as it indicates the magnitude of the mobility change that occurs with differences in drift gas polarizability. It is this factor that enables the use of different drift gases to change separation factors, as it is at least theoretically possible to separate two compounds with different slopes using an appropriate drift gas.

CHAPTER THREE

GENERATION AND ANALYSIS OF CANDIDATE STRUCTURES

Ensembles of conformations that explore the potential energy surface for α- and β-[methyl-D-mannopyranoside]-Na$^+$ were generated by varying ring conformation and cation location relative to the ring. The respective geometries were optimized using density functional theory (B3LYP) with the 6-31G* basis set. Relative energies and radii of gyration were then determined. Neutral structures were analyzed using simulated annealing molecular dynamics and single-point energy calculations for purposes of comparison to the lowest-energy conformers of their Na$^+$ adducts.

I. Computational Methods

Molecular mechanics and density functional theory have been employed to explore the conformational potential energy surfaces of neutral and sodiated methyl glycoside species.

A. Molecular Mechanics Methods

Molecular mechanics methods use the laws of classical physics to predict molecular properties and structure. Rather than calculating electronic structure, molecular mechanics calculations examine interactions among nuclei. These interactions are characterized by force fields consisting of three components: 1) an equation defining the dependence of a molecule's potential energy on the locations of its atoms; 2) a series of atom types that define the hybridization and bonding behavior of an atom of a particular element; and 3) a parameter set that fits the equation and atom types to experimental data.

Parametrization based on experimental data is particularly important in molecular mechanics, as it allows for the implicit inclusion of electronic effects in force fields. Because molecular mechanics methods do not explicitly consider electronic structure, they are computationally inexpensive; this permits researchers to efficiently examine a wide variety of potential conformations. Here the CHARMM molecular mechanics

program is used to quickly assess the possible geometries of a molecule with many conformational degrees of freedom.

CHARMM Force Field

The CHARMM22 all-atom force field uses a potential that takes into account both covalent and noncovalent interactions. The form of the potential is

$$U(\vec{R}) = \sum_{bonds} K_b(b-b_0)^2 + \sum_{UB} K_{UB}(S-S_0)^2 + \sum_{angle} K_\theta(\theta-\theta_0)^2 +$$
$$\sum_{dihedrals} K_\chi(1+\cos(n\chi-\delta)) + \sum_{impropers} K_{imp}(\varphi-\varphi_0)^2 + \quad\quad (3.1)$$
$$\sum_{nonbond} \varepsilon\left[\left(\frac{R_{min,ij}}{r_{ij}}\right)^{12} - \left(\frac{R_{min,ij}}{r_{ij}}\right)^6\right] + \frac{q_i q_j}{\varepsilon_1 r_{ij}}$$

where $\vec{R}$ is the vector of the coordinates, $b, S, \theta, \chi,$ and φ are bond length, Urey-Bradley 1,3-nonbonded interaction distance, bond angle, dihedral angle, and improper torsion angle (subscript zero indicates equilibrium value), respectively, and $K_b, K_{UB}, K_\theta, K_\chi,$ and K_{imp} are bond, Urey-Bradley, angle, dihedral, and improper dihedral force constants.

Non-bonded interactions (electrostatic and van der Waals) are described by Coulombic and Lennard-Jones (6-12) potentials, described by the last two terms in Eq. 3.1. In the Lennard-Jones (LJ) term, ε represents the potential energy well depth and R_{min} represents the interatomic distance at potential energy minimum. In the Coulombic term, q represents partial atomic charge, ε_1 the effective dielectric constant (set to unity), r_{ij} the interatomic distance between atoms i and j. The values of the LJ parameters between different atoms i and j are obtained according to the Lorentz-Berthelot combination rules; ε_{ij} is the geometric mean of ε_i and ε_j, and $R_{min\ ij}$ is the arithmetic mean of $R_{min\ i}$ and $R_{min\ j}$.

Several options are available for calculating the nonbonded energy terms. In principle, they should be calculated pairwise, however, the number of terms increases with the square of the number of atoms (N^2), making this method very computationally

expensive. In order to speed up computation, interactions between two atoms separated by a distance greater than a predefined cutoff distance are neglected.

Running CHARMM

Four files are required to run any CHARMM calculation. They include the residue topology file (RTF), the parameter file (PARAM), the coordinate file (COOR), and the protein structure file (PSF):

- The residue topology file contains atom type information (name and atomic mass) used to define an atom in a particular bonding situation; a list of hydrogen bond donors and acceptors; the partial charge of each atom; and a description of the atoms' connectivity.

- The parameter file contains the experimental parameters needed for calculating molecular energy—the equilibrium bond distances and angles for bond stretching, angle bending and dihedral terms in the CHARMM potential, force constants, and LJ 6-12 potential parameters. Parameters are associated with particular atom types defined in the topology file.

- The coordinate file consists of the Cartesian coordinates for each atom in the system.

- The protein structure file is generated from the information contained in the RTF file. The PSF is the most fundamental CHARMM data structure; it must be specified before calculations are performed on the molecule.

Topology and parameter files contain information for a particular class of molecules, such as carbohydrates, nucleic acids, or proteins, while the protein structure file (PSF) is generated for specific molecules.

Simulated Annealing Molecular Dynamics

The conformational potential energy surfaces of neutral methyl-D-hexopyranoside anomers were explored using molecular dynamics (MD) simulations in CHARMM. In MD simulations, a series of molecular configurations are generated by integration of Newton's laws of motion, relating the mass and acceleration of each atom to the gradient of the potential energy as described by the molecular mechanics force field. This generates a trajectory describing how the velocities and positions of the atoms in the system vary with time.

One possible application of molecular dynamics is simulated annealing (SAMD) (Kirkpatrick et al 1983); this method is named in analogy to annealing—the process in which a molten substance is slowly cooled until the material forms a single crystal. The basic characteristic of the annealing process is the use of careful temperature control; the crystal eventually obtained corresponds to the global energy minimum. In simulated annealing, this process is imitated in order to find the lowest energy structure for a system with a large number of low-energy minima on the potential energy surface.

A modification of the simulated annealing molecular dynamics protocol developed by Hill et al (2002) was implemented to obtain the most likely conformation for the neutral methyl-D-hexopyranoside anomers in the desolvation region where the Na^+ adducts are formed. A temperature of 473 K (200 °C) was employed as the final temperature.

In the simulations of the neutral methyl-D-hexopyranoside anomers, the RTF files for first-cycle starting structures were constructed using Mulliken atomic charges derived from DFT calculations (*vide infra*), and the initial coordinate (PDB) files were constructed using the DFT-optimized geometries which represented the local minima

used as starting structures for the series of simulated annealing cycles. The CHARMM 22 all-atom parameters for carbohydrates (Ha et al 1988) were used.

The simulated annealing protocol (Quinton 2006) consists of a series of steps, beginning with heating from 0 K to 1000 K in 2 K increments over a period of 500 ps to remove conformational restraints. This step is followed by an equilibration step of 300 ps with a 5 K temperature window. The molecules are then cooled from 1000 K to 473 K, in increments of 0.2565 K, over a period of 2000 ps. The cooling step is followed by a second 300 ps equilibration step with an identical temperature window.

The final production step, in which the motions of the molecule are traced at the final temperature (473 K) to generate the set of coordinate frames representing its atoms' trajectory over time, occurs over a period of 2000 ps. For all steps, a leapfrog Verlet integrator (Hockney 1970) with a time-step of 1 fs was used.

At the end of each cycle, the structure with the lowest energy is obtained; it then becomes the seed for the next cycle. A second search algorithm is used to obtain the energy and radius of gyration of the lowest-energy conformation for each cycle. The lowest-energy structure from all ten cycles is considered to be the best representation of the conformation at the temperature of the desolvation region.

While the SAMD method produced reasonable structures for the neutral methyl-D-hexopyranosides; highly unphysical geometries were obtained during trial runs with Na^+ adducts, as discussed in Chapter 4.

B. Density Functional Theory

Density functional theory (DFT) is distinct from wave function-based methods such as Hartree-Fock theory in that it describes the electronic structure of molecules in terms of their electron density ρ rather than their many-body wave function. As ρ describes the

likelihood of finding an electron in a particular volume of space, it is a function of x, y, and z coordinates. Thus, for an N-electron molecule, the basic variable of the system depends on only three degrees of freedom rather than the 3N degrees of freedom of a wavefunction-based method. For this reason, DFT is mathematically simpler, so it can be applied efficiently to larger systems than Hartree-Fock and other wavefunction-based methods.

In DFT, the total electronic energy is treated as a function of ρ, which in turn is a function of x,y, and z. Thus, the energy is a functional (a function whose domain is also a set of functions.) Following the work of Kohn and Sham (1965) the approximate functionals take the form of

$$E = E^T + E^V + E^J + E_{xc}, \tag{3.2}$$

where E^T is the kinetic energy term arising from electron motion, E^V is a combined term that describes the potential energy of nuclear-electron attraction and nuclear-nuclear repulsion, E_J is the electron-electron (Coulomb) repulsion term, and E_{xc} is the exchange-correlation term. All terms except the nuclear-nuclear repulsion are functions of ρ; $E^T + E^V + E^J$ corresponds to the classical energy of the charge distribution, while E_{xc} accounts for the exchange energy due to the antisymmetry of the quantum wave function and dynamic correlation in individual electrons' motion.

Hohenberg and Kohn (1964) demonstrated that E_{xc} is a functional of the electron density, so applications of DFT are based on approximations for the exchange-correlation potential; the exact exchange-correlation potential is unknown. E_{xc} is divided into exchange and correlation components; each component is also a functional of the electron density. Exchange and correlation functionals (E_x and E_c) can be of two distinct types: local functionals dependent only on the electron density ρ (these are said to follow the

local density approximation or LDA) while gradient-corrected functionals depend on both ρ and the density gradient $\nabla\rho$. Approximations of E_{xc} including a correction for the density gradient are defined within the generalized-gradient approximation (GGA).

The B3LYP density functional theory method used here includes two generalized-gradient approximations:

- Becke's three-parameter exchange functional (B3P), which incorporates both DFT and Hartree-Fock exchange, giving the method its "hybrid" character (Becke 1993).

- The gradient-corrected Lee-Yang-Parr (LYP) correlation functional which computes the total correlation energy rather than correcting the LDA expression (Lee, Yang, and Parr 1988).

The B3LYP model defines the exchange-correlation energy E_{xc} as

$$E_{xc}{}^{B3LYP} = (1-a)E_x{}^{LSDA} + aE_x{}^{HF} + b\Delta E_x{}^{B} + (1-c)E_c{}^{LSDA} + cE_c{}^{LYP} \qquad (3.3)$$

where a, b, and c are Becke's three empirically-derived parameters; $E_x{}^{LSDA}$ is the local spin-density approximation exchange functional (LSDA is an extension of the LDA which takes into account spin polarization); $E_x{}^{HF}$ the HF exchange functional; $E_c{}^{LSDA}$ the LSDA correlation energy, computed using the VWN3 or Vosko-Wilk-Nussair LSDA correlation functional (Vosko, Wilk, and Nussair 1980) and $E_c{}^{LYP}$ the LYP correlation energy.

C. Geometry Optimization Using Electronic Structure Methods

Geometry optimization is based on the concept of the potential energy surface, which describes the energy of the molecule as a function of atomic or nuclear positions. (According to the Born-Oppenheimer approximation, as nuclei are much larger and move more slowly than electrons, the electron distribution depends solely on the positions, not

the velocities, of the nuclei.) The lowest-energy molecular geometry corresponds to a minimum or valley on the potential energy surface. The first derivatives of the potential energy surface with respect to the positions of the atoms or nuclei are known as the gradients; the forces acting on the atoms or nuclei are the negatives of the gradients. Locations at which the forces and gradients are zero are called stationary points; these can correspond to minima, transition states (first-order saddle points) and higher-order saddle points.

The first derivatives are insufficient for distinguishing between minima and saddle points; second derivatives are required for this purpose. The matrix of second derivatives of the potential energy surface is known as the Hessian or force-constant matrix $\mathbf{H}$. If the Hessian is transformed to mass-weighted coordinates and diagonalized, the eigenvectors are the vibrational normal modes and the eigenvalues are proportional to the vibrational frequencies.

For the potential energy surface to have a minimum with respect to any coordinate, its second derivative with respect to that coordinate must be positive. A stationary point that describes the lowest-energy molecular geometry must be a minimum in all directions, so that it must have positive eigenvalues for all modes; this means that a molecule at a minimum can have only real vibrational frequencies.

A variety of algorithms are available for geometry optimization; Within the Gaussian 03 software, a quasi-Newton algorithm known as the "Berny" optimization algorithm (Schlegel 1982) is employed. Quasi-Newton methods assume a quadratic form for the potential energy surface; beginning with an approximate Hessian $\mathbf{B,}$ they improve the quadratic model by updating the estimated Hessian $\mathbf{B}$ or its inverse $\mathbf{B^{-1}}$ through the course of the optimization. At each given step, the approximate Hessian or its inverse must allow

a fit between the quadratic model and the gradient at the current and previous points. This requirement is known as the quasi-Newton or secant condition.

D. Calculation of Radius of Gyration

The radius of gyration (R_g), defined as

$$R_g = \sqrt{\frac{1}{N_i}\sum(r_i - r_{cm})^2} \qquad (3.4)$$

where N_i is the number of atoms in the ion and $r_i - r_{cm}$ is the distance between any atom 'i' and the ion's center of mass, is considered to be an average radius for the ion in the absence of other molecules and a useful measure of the ion's size and compactness. R_g values were calculated from Cartesian coordinates of the DFT-optimized structures using the coordinate analysis facility of the CHARMM program.

II. Generation of Candidate Structures

Pyranosyl Conformations. Pyranosyl rings can adopt four basic conformations: chair, boat, skew-boat, and half-chair, designated *C*, *B*, *S*, and *H* respectively. The conformations are assigned by first choosing a reference plane containing four ring atoms. If an unequivocal choice cannot be made, the reference plane is chosen so that the lowest-numbered ring carbon is displaced from the plane. Ring atoms located above the reference plane are written as superscripts preceding the letter corresponding to one of the five basic conformations; those located below the reference plane are written as subscripts following the letter. Pyranosyl rings can adopt 2 chair conformations, 6 boat conformations, 6 skew, 12 5-atom planar half-chair (envelope or E), and 12 4-atom planar half-chair conformations yielding a total of 38 conformations in all (Rao et al 1998).

The energy distribution of these conformers differs among the aldopyranoses (Dowd et al 1994); the $^4C_1$ chair conformation is predicted to be dominant for the majority of aldopyranose species, including those whose methyl glycosides are considered in this study.

Generation of Candidate Structures. The strategy of generating an ensemble of conformers for the [methyl-D- hexopyranoside]-Na$^+$ complexes was based on that used by Cerda and Wesdemiotis (1999) in their computational study of monosaccharide-Na$^+$ complexes. For each α- and β-anomer, the eight basic chair and boat conformations ($^4C_1$ and $^1C_4$ chair forms and $^{2,5}B$, $B_{2,5}$, $^{0,3}B$, $B_{0,3}$, $^{1,4}B$ and $B_{1,4}$ boat forms) of the pyranose ring were considered. Other conformations, such as the half-chair (*H*) and skew-boat (*S*), were omitted from consideration. Half-chair conformations are highly strained and correspond to maxima on the potential energy surface for the pyranosyl ring (Dowd et al 1994). Skew-boat forms correspond to intermediates between different boat structures (Shallenberger 1982).

At each conformation, Na$^+$ attachment above and below the ring was considered, provided that the structure afforded the possibility of coordination in a multidentate (≥2) manner, as predicted by the Na$^+$ affinities that have been determined for monosaccharide stereoisomers.

Geometry Optimization. Geometries of neutral and sodiated structures were optimized using the B3LYP hybrid density functional method with a 6-31G* basis set. The B3LYP method has been found to be well-suited for studying ion-molecule complexes (Hoyau and Ohanessian 1997) and intramolecular hydrogen bonds (Gonzalez et al 1997) which are characteristic of monosaccharides.

The Gaussian 03 program was used in all calculations; in each case, the standard "Berny" optimization algorithm and standard convergence criteria were employed. Vibrational frequency calculations were performed to verify that optimized structures correspond to genuine minima on the potential energy surface (a minimum can be defined as a structure whose vibrational frequencies are all real.) The total electronic energies of each optimized structure along with zero-point energy (ZPE) corrections were obtained in each case.
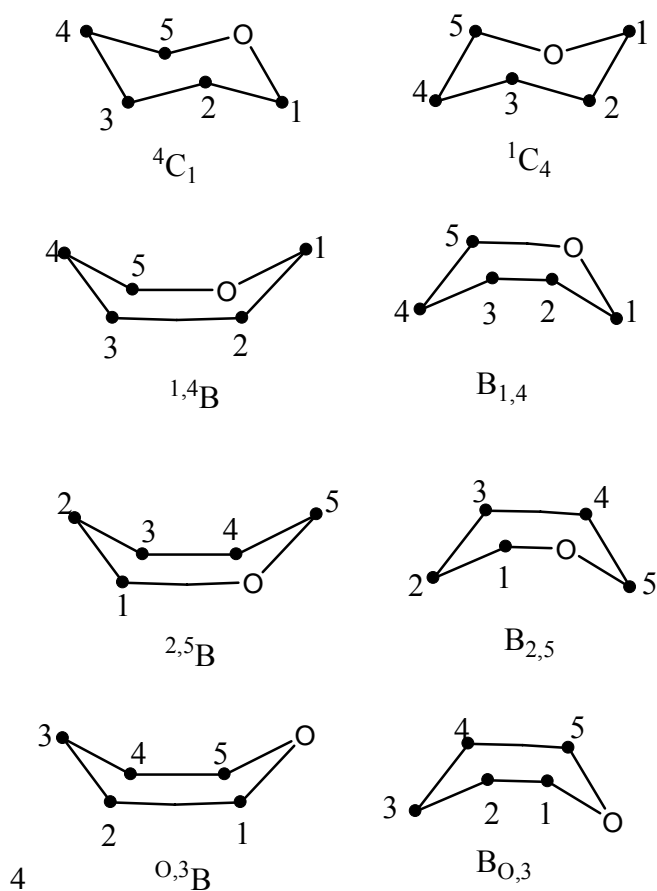
Figure 3.1 Pyranose ring conformations used to generate an ensemble of conformers for the sodiated adduct.

Conformational Analysis of Neutral Methyl-D-Hexopyranosides

Neutral structures for both anomers of each methyl-D-hexopyranoside were started in the $^4C_1$ chair conformation which allows the largest number of equatorial substituents.

Both computational studies (Vijayalakshmi et al 1973) and NMR studies (Bock and Pedersen 1983) have demonstrated that the $^4C_1$ chair conformation is the dominant form. Neutral methyl-D-hexopyranoside anomers were geometry optimized in Gaussian 03 using the same B3LYP/6-31G* level of theory as the Na^+ adducts. Coordinates and Mulliken charges (*vide infra*) of these optimized structures were used to generate starting structures for simulated annealing molecular dynamics (SAMD) conformational studies performed in CHARMM.

CHAPTER FOUR

RESULTS AND DISCUSSION

The size and conformation of neutral and sodiated methyl-D-mannopyranoside anomers is described, as is the determination of the energy barrier for ring hydroxyl conformational change in the α anomer. It is shown that the [methyl-D-mannopyranoside]Na$^+$ complex retains the $^4C_1$ chair ring conformation of the neutral species. Radii for [MeMan]Na$^+$ complexes determined from the application of the zero-polarizability approximation to experimental data are compared with those calculated from the lowest-energy theoretical structures. While the experimental radii are larger, experimental and theoretical data agree on the relative sizes of the two anomers. Dipole moments were also calculated and compared for α and β anomeric forms of MeMan]Na$^+$ as a first step in understanding the interactions of the complexes with drift gases of varying polarizability.

I. Neutral Structures

A. Hydroxymethyl and Hydroxyl Rotamers

The orientation of the hydroxymethyl (CH$_2$OH) group relative to the pyranose ring is

described in terms of three conformers arising from internal rotation about the C5-C6

bond, designated trans-gauche (*TG*), gauche-gauche, (*GG*), and gauche-trans (*GT*)

(Sundaralingam 1968). In this terminology, the orientation of the hydroxymethyl C6-O6

bond relative to the C5-O5 bond (measured by the O6-C6-C5-O5 dihedral) is stated first,

followed by its orientation relative to the C4-C5 bond (measured by the O6-C6-C5-C4

dihedral). In this study, a modified form of the nomenclature introduced by Cramer and

Truhlar (1993) is used to describe the conformation of ring hydroxyl groups (Figure 4.1).

The letters *g+*, *g-*, and *t* are used to indicate whether the H-O-C(*n*)-C(*n − 1*) dihedral is

gauche-clockwise (*g+*), gauche-counterclockwise (*g-*), or trans (*t*), where clockwise and

counterclockwise refer to the direction of the rotation of the hydroxyl group required to

eclipse the C(*n*)-C(*n − 1*) bond. In this study, a three-letter descriptor is employed, in

which the order of the letters corresponds to the hydroxyl groups at C2, C3, and C4.

B. Intramolecular Hydrogen Bonding

As there are three different rotamers for each hydroxyl group and for the hydroxymethyl group, there are literally hundreds of possible conformers just for a single anomeric form in the $^4C_1$ chair arrangement. Not all the conformers are of equal stability; the most stable are those in which the ring hydroxyl groups are arranged so as to maximize intramolecular hydrogen bonding (Brady and Schmidt 1993).
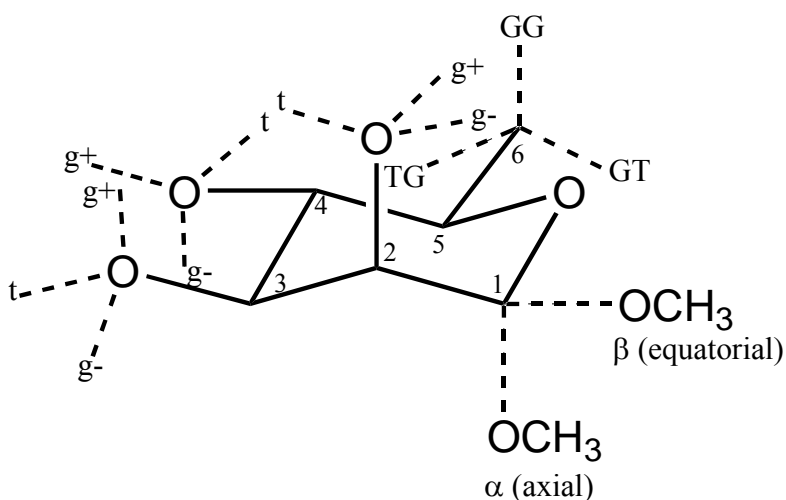
Figure 4.1: Conventions for labeling the hydroxymethyl and hydroxyl rotamers of methyl-D-mannopyranoside. The methyl group is not considered in this scheme as it does not participate in hydrogen bonding.
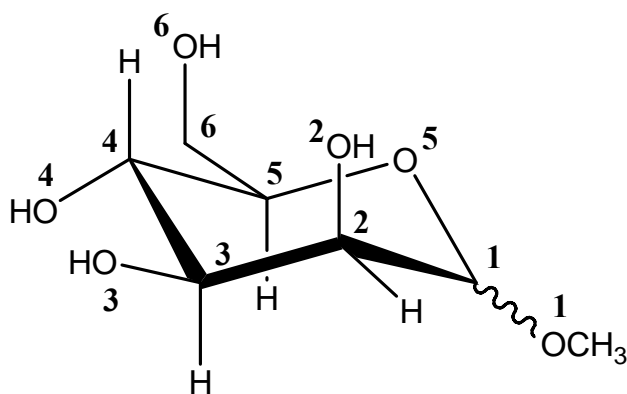
Figure 4.2: Numbering of heavy atoms in methyl-D-mannopyranoside. Oxygen atoms are numbered according to the carbon to which they are attached.

33

Hydrogen bonding is generally defined as an "X-H---A" local bonding arrangement in which X-H serves as a proton donor to A (Steiner 2002). In the case of carbohydrates, X and A are both oxygen atoms, so that intramolecular hydrogen bonds in a carbohydrate molecule can be designated Oi-H---Oj, where i and j are the numbers of the donor and acceptor oxygen atoms (Figure 4.2). In this study, hydrogen bonds are identified using the criteria suggested by Steiner and Saenger (1992)—$d_{H---O} < 3.0$ Å and $\alpha_{OH---O} > 90°$—based on analysis of neutron diffraction data from carbohydrates.
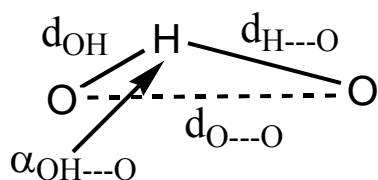
Figure 4.3: Schematic illustration of hydrogen-bond parameters: d_{H---O} = H---O distance, α_{OH---O} = O-H---O angle (after Steiner and Saenger 1992). Due to trigonometric relations, only three of the four parameters are independent; if d_{OH} is regarded as essentially constant (~0.97 Å), only two independent parameters remain.

C. Description of Neutral Structures

A set of ten structures for each of the two methyl-D-mannopyranoside anomers were generated by simulated annealing molecular dynamics using CHARMM. Single-point energies for each structure were calculated using DFT at the B3LYP/6-31G* level, indicating broad energy distributions for the SAMD structures (approximately 7.0 kcal/mol for the α anomers and 6.3 kcal/mol for the β anomers.) Geometry optimizations, also at the B3LYP/6-31G* level, were performed on each simulated-annealing structure, upon which the ten SAMD structures obtained for each anomer converged to single distinct minima for the α and β forms. The fact that twenty starting structures converged to two distinct minima, one for each anomeric form (Figures 4.4 and 4.5) is an indication that the structures obtained can be regarded as global, rather than local, minima on the conformational potential energy surface.

As expected, the ring is in the stable $^4C_1$ chair form in both anomeric forms. As displayed in Figures 4.4 and 4.5, both anomers show the hydroxymethyl group in the GG conformation, consistent with crystallographic and NMR studies showing that the relative population of GG, TG, and GT rotamers is dependent on the configuration of the hydroxyl group at C4 (Marchessault and Perez 1979, Nishida et al 1988, Hori et al 1990). These studies indicate GG is the most populated conformer when O4 is equatorial, as in glucose and mannose.
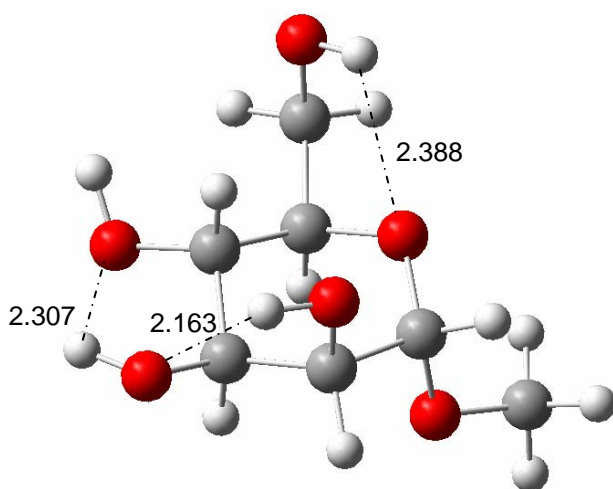
Figure 4.4 The most stable structure optimized for methyl-α-D-mannopyranoside (α-MeMan) at B3LYP/6-31G* level. Hydrogen bond lengths (in dotted lines) are in Å.
Color scheme: red = oxygen; gray = carbon; white = hydrogen
R_g = 2.731 Å.

In the α anomer (Figure 4.4) the intramolecular hydrogen bonds are all clockwise: O6-H---O5, O2-H---O3, and O3-H---O4 (hydrogen bond lengths are given in Figure 4.3), giving a *ttt* ring hydroxyl conformation. The β anomer (Figure 4.5) shows counterclockwise hydrogen bonding involving the ring hydroxyl groups— O2-H---O1, O3-H---O2, O4-H---O3, giving a *g-g+g+* ring hydroxyl conformation—and clockwise O6-H---O5 for the hydroxymethyl group. These patterns are consistent with the

prediction that the most stable rotamers of a given monosaccharide are those that exhibit multiple consecutive intramolecular hydrogen bonds.
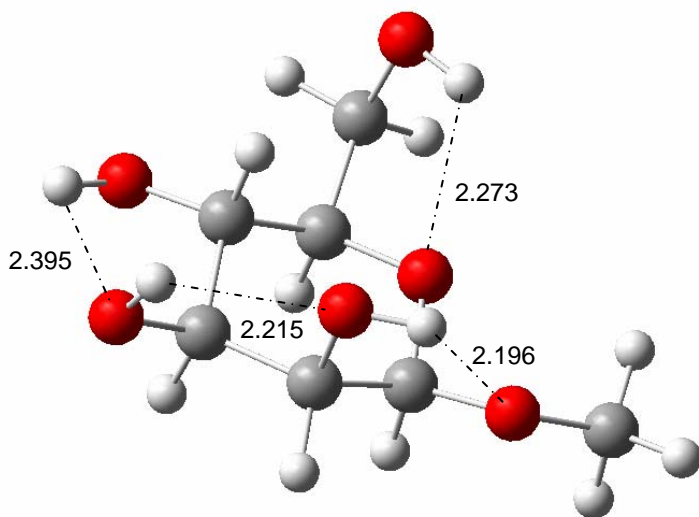
Figure 4.5 The most stable structure optimized for methyl-β-D-mannopyranoside (β-MeMan) at B3LYP/6-31G* level. Hydrogen bond lengths (in dotted lines) are in Å.
Color scheme: red = oxygen; gray = carbon; white = hydrogen.
R_g = 2.737 Å.

II. Conformational Analysis of Sodiated Structures

A. Lowest-Energy Structures

Figure 4.6 shows the lowest-energy structure for α-[MeMan]Na$^+$, wherein the monosaccharide binds the cation in a tridentate fashion, with the participation of the axial hydroxyl oxygen O2, the ring oxygen O5, and the hydroxymethyl oxygen O6. In the lowest-energy structure for β-[MeMan]Na$^+$, the binding is tetradentate, as the equatorial methoxy oxygen O1 participates in addition to O2, O5, and O6. These coordination schemes, along with the $^4C_1$ conformation of the pyranose ring, closely match structures previously calculated for the Na$^+$ complexes of α- and β-mannose using *ab initio* methods at a HF/6-31G* level of theory (Cerda and Wesdemiotis 1999).

36

a)

tg-g+/GG

b)
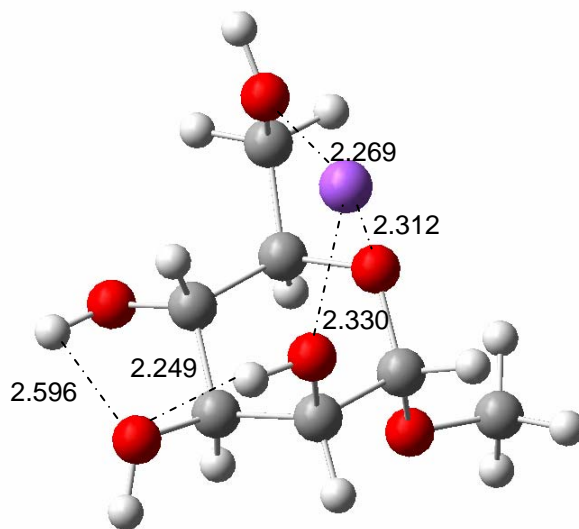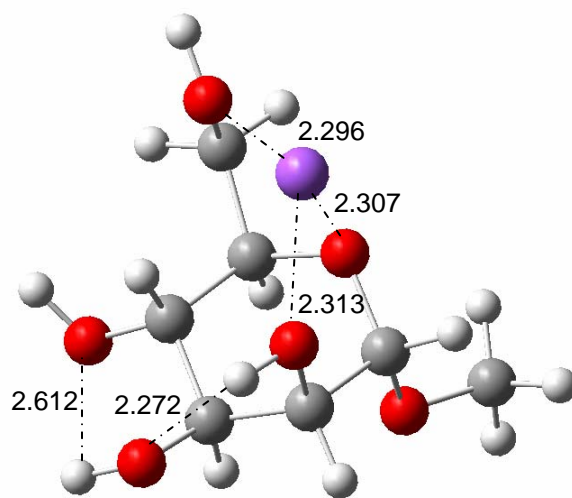
ttt/GG

Figure 4.6 The two lowest-energy ($^4C_1$ chair) structures for α -[MeMan]Na$^+$:
Rotamer designations are given below each structure. Colors used to designate the atoms:
red= oxygen, gray = carbon, white = hydrogen, purple = sodium.
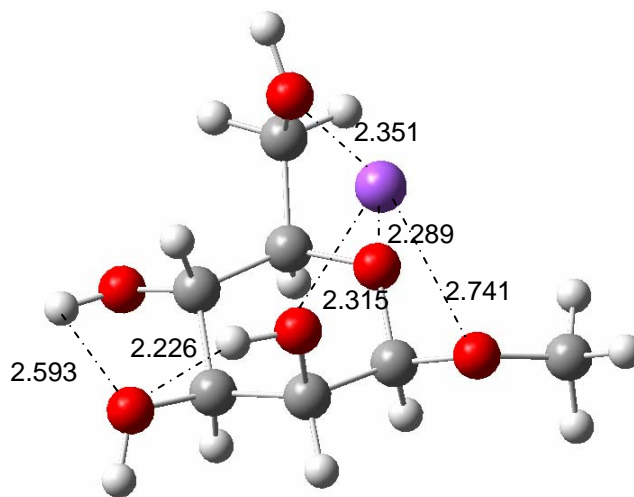
tg-g+/GG

Figure 4.7 The lowest-energy ($^4C_1$ chair) structure for β -[MeMan]Na$^+$. Rotamer designation is given below the structure. Colors used to designate the atoms: red = oxygen, gray = carbon, white = hydrogen, purple = sodium.

Coordination Site

As shown in Figures 4.6 and 4.7, the Na$^+$-O2, Na$^+$-O5, and Na$^+$-O6 bonds for both α

and β structures are of similar length, all approximately 2.25 – 2.35 Å, making the

coordination site in the tridentate α structures approximately symmetric. In the

tetradentate β structure, the Na$^+$-O1 interaction is approximately 2.74 Å, significantly

longer and presumably weaker than the other three bonds, making this structure's

coordination site asymmetric.

In an attempt to characterize the interactions between the cation and the oxygen

ligands, Mayer bond order analysis (Mayer 1984) was performed on the lowest-energy α

and β structures using Gaussian 03. Mayer bond order is related to the number of shared

electron pairs between the atoms; it thus describes the degree of covalency of a particular

bond (Bridgeman and Cavigliasso 2003).

Table 4.1 shows that the bond order between Na^+ and O1 in the β anomer complex is significantly lower than the other bond orders, consistent with the greater length of the Na^+-O1 bond relative to the other three Na^+-O bonds. The greater length and lower bond order indicates that the Na^+-O1 interaction is weaker than the other three Na^+-O interactions in the β anomer complex . A slight difference was also observed between the Mayer bond orders of the Na^+-O2 and Na^+-O6 bonds and that of the Na^+-O5 bond (0.16 – 0.17). As there is no significant difference in bond length between Na^+-hydroxyl oxygen and Na^+-pyranose ring oxygen bonds, this may be accounted for by differences in charge distribution (as measured by Mulliken population analysis) between oxygen atoms in different environments; the greater negative charges on the O2 and O6 hydroxyl groups indicate that they have slightly more electron density to share with the cation.

Table 4.1 Mayer bond orders and bond lengths for Na^+-O bonds and charge distribution obtained from Mulliken population analysis.

Alpha				
Bond	Bond order	Bond length	Charge distribution	
Na+-O6	0.200	2.269	Na+	0.638
Na+-O5	0.171	2.312	O6	-0.659
Na+-O2	0.205	2.330	O2	-0.662
			O5	-0.535
Beta				
Bond	Bond Order	Bond length	Charge distribution	
Na+-O6	0.185	2.741	Na+	0.618
Na+-O5	0.156	2.289	O6	-0.650
Na+-O2	0.186	2.315	O2	-0.655
Na+-O1	0.118	2.351	O5	-0.533
			O1	-0.470

Previous *ab initio* studies have shown that the interaction of Na^+ with various ligands tends to be largely electrostatic (Guo et al 1989). The relatively low Na^+-O bond orders (0.1 – 0.2, versus 0.8 – 1.0 for covalent C-O and C-C bonds) obtained through Mayer bond order analysis are consistent with the primarily electrostatic character of Na^+-O interactions, but Mayer bond order analysis indicates that the Na^+-O bonding interaction has a covalent component that can be as high as 20 percent.

Intramolecular Hydrogen Bonding and Rotamer Distribution

The lowest-energy β and two lowest-energy α structures show two intramolecular hydrogen bonds involving the ring hydroxyls O2, O3, and O4; the lengths of the two bonds are roughly identical in α and β structures. The lower-energy α structure (Na^+-αMeMan1) and the β structure (Na^+-βMeMan1) show hydrogen bonds O2-H---O3 and O4-H---O3, giving a *tg-g+* ring hydroxyl conformation (Figure 4.6a, Figure 4.7). In the higher-energy α structure (Na^+-αMeMan10) the donor and acceptor roles of O3 and O4 are reversed, giving the hydrogen bond O3-H---O4 and a *ttt* ring hydroxyl conformation (Figure 4.6b).

Given that Na^+-αMeMan1 and Na^+-αMeMan10 are nearly identical in aspects other than ring hydroxyl conformation, and differ in thermodynamic stability by only 1.420 kcal/mol under experimental conditions(Table 4.2), the population of the *ttt* state is likely to be determined by the energy barrier of interconversion between the two rotamers. The transition state of the *tg-g+* → *ttt* conversion for the α anomer was located using the synchronous transit guided quasi-Newton (QST2) method implemented in Gaussian 03 (Peng and Schlegel 1993) and verified using a frequency calculation. A comparison of single point-energies (Table 4.4) between the lower-energy *tg-g+* structure and the transition state structure indicated an energy of activation (E_a) of approximately 1.84

kcal/mol for this interconversion. Application of the zero-point correction to the energy of the transition state indicated that the *tg-g+* → *ttt* transition lacks a kinetic barrier. As the relative energy is not significantly greater than *kT* under experimental conditions, it is likely that, at least in α-[MeMan]-Na$^+$, both the *tg-g+* and *ttt* rotamers are populated.

Table 4.2 Absolute and relative single-point energies of *tg-g+* and *ttt* structures of α-[MeMan]-Na$^+$, calculated at B3LYP/6-31G* level of theory.

	E (hartrees)	ΔE_{rel} (kcal/mol): uncorrected	ΔE_{rel} (kcal/mol): ZPE and thermal correction at 473 K
tg-g+ (Na$^+$-αMeMan1)	-888.6359046	0	0
Transition state	**-888.6329789**	**1.836**	**-0.198**[a]
ttt (Na$^+$-αMeMan10)	-888.6333490	1.603	1.420
kT (473 K)		0.942	

[a] Zero-point correction only.

Radii of Gyration

As expected, the radii of gyration (R_g) for the sodiated structures are greater than those of the neutral structures. However, the key property for a study of IMS separation is not intrinsic R_g values, but the difference in R_g values between the two species being separated. While the difference in R_g values between the two anomers is significantly greater in the sodiated form than in the neutral form, the lowest-energy sodiated structures' radii of gyration differ by less than 2% (Table 4.3).

Table 4.3 Radii of gyration (R_g) for neutral and sodiated methyl-D-mannopyranoside anomers (all values in Å).

	Neutral	Sodiated
α-MeMan	2.731	2.762 (tg-g+) 2.761 (ttt)
β-MeMan	2.737	2.816
R_g (β) - R_g (α)	0.007	0.054 – 0.055

The small size of this difference is consistent with the retention of the stable $^4C_1$ chair and GG hydroxymethyl conformation in both α and β sodiated structures.

B. Oxygen Coordination and Ring Conformation

For both α and β anomers, bidentate structures are the highest in energy. Tridentate structures in which the hydroxymethyl oxygen does not participate in binding the cation are also highly unfavorable (Tables 4.4 and 4.5). The energies of bidentate structures are all above 17 kcal/mol relative to the lowest-energy conformation, while tridentate structures in which the hydroxymethyl group does not participate in binding the cation have energies above 14 kcal/mol. This is consistent with previous theoretical work indicating that monosaccharides prefer to coordinate alkali- or alkaline-earth metals in a tri- or tetradentate arrangement (Zheng et al 1997, Cerda and Wesdemiotis 1999, Botek et al 2001) and experimental evidence that the availability of the hydroxymethyl group for cation coordination accounts for the greater Na^+ affinity of hexoses relative to pentoses (Cerda and Wesdemiotis 1999). It is also noteworthy that all tri- or tetradentate structures include the pyranose ring oxygen as one of the coordinating atoms (Tables 4.4 and 4.5).

DFT results indicate that in the α anomer, tridentate coordination is favored (all but three of the fourteen α-MeMan-Na^+ structures listed in Table 4.4 are tridentate, including the two lowest-energy structures). It is also clear that the Na^+ cation prefers to bind above the pyranose ring, as tridentate structures in which the axial O1 oxygen participates in binding the cation (Na^+-αMeMan9 and Na^+-αMeMan12) are unfavorable, with relative energies above 9.8 kcal/mol. In the β anomer, tetradentate coordination is favored (most of the structures listed in Table 4.5, including the lowest-energy structure, are tetra-dentate) as the equatorial position of O1 allows it to bind the Na^+ cation above the pyranose ring.

Table 4.4 Absolute and relative energies and coordinating atoms for α-MeMan-Na$^+$ conformers obtained at the B3LYP/6-31G* level of theory (only structures with relative energies below 25 kcal/mol are shown). The most stable conformers are in boldface.

	Coordinating oxygen atoms	E(hartrees)*	ΔE_{rel} (kcal/mol)
Na$^+$-αMeMan1	**O5, O6, O2**	**-888.407808**	**0**
Na$^+$-αMeMan2	O5, O6, O1	-888.392079	9.870
Na$^+$-αMeMan3	O3, O4	-888.373245	21.689
Na$^+$-αMeMan4	O6, O2, O3	-888.380717	17.000
Na$^+$-αMeMan5	O1, O4, O5	-888.385423	14.047
Na$^+$-αMeMan6	O5, O6, O3	-888.400077	4.851
Na$^+$-αMeMan7	O1, O4	-888.373352	21.621
Na$^+$-αMeMan8	O5, O2, O6	-888.385885	13.757
Na$^+$-αMeMan9	O1, O4, O5	-888.376714	19.512
Na$^+$-αMeMan10	**O5, O6, O2**	**-888.405505**	**1.445**
Na$^+$-αMeMan11	O5, O6, O3	-888.400384	4.659
Na$^+$-αMeMan12	O5, O6, O1	-888.391455	10.262
Na$^+$-αMeMan13	O5, O6, O2, O3	-888.395096	7.977
Na$^+$-αMeMan14	O1, O4	-888.378569	18.348

*Corrected for zero-point energy.

In addition to the energetic favorability of tri- or tetradentate binding, DFT calculations also indicated that the conformation of the pyranose ring played a significant role in determining the relative energies of the sodiated structures. In the α anomer, tridentate boat and skew-boat structures, a tridentate $^1C_4$ chair structure and a tetradentate boat structure are at least 3.2 kcal/mol higher in energy than tridentate $^4C_1$ chair structures (Table 4.4). Likewise, in the β anomer, tetradentate boat and skew-boat structures are higher in energy than tetradentate $^4C_1$ chair structures by at least 4 kcal/mol

(Table 4.5). These results indicate that both anomeric forms of methyl-D-mannopyranoside (MeMan) retain the stable $^4C_1$ chair conformation of their neutral forms when complexed with Na^+. Previous theoretical studies of the Na^+ complexes of Glc, Gal, and Man (Cerda and Wesdemiotis 1999) indicates that retention of the $^4C_1$ chair form may be due to the axial orientation of the hydroxyl group at C2, which permits tri- or tetradentate coordination of the cation in the $^4C_1$ chair conformation.

Table 4.5 Absolute and relative energies and coordinating oxygen atoms for β-MeMan-Na^+ conformers obtained at the B3LYP/6-31G* level of theory (only structures with relative energies below 25 kcal/mol are shown). The most stable conformers are in boldface.

	Coordinating oxygen atoms	E (hartrees)*	ΔE_{rel} (kcal/mol)
Na^+-βMeMan1	**O5, O6, O1, O2**	**-888.409421**	**0**
Na^+-βMeMan2	O3, O4	-888.382097	17.146
Na^+-βMeMan3	O5, O6, O3, O1	-888.401813	4.774
Na^+-βMeMan4	O5, O6, O2, O3	-888.396302	8.232
Na^+-βMeMan5	O5, O6, O1, O2	-888.399874	5.991
Na^+-βMeMan8	O5, O6, O2, O3	-888.403073	3.983
Na^+-βMeMan9	O1, O5, O3	-888.382980	16.592

*Corrected for zero-point energy.

In the β anomeric form, the methoxyl O1 and the hydroxyls O2 and O3 form an equatorial-axial-equatorial sequence, which allows tetradentate coordination of the cation without significant strain on the $^4C_1$ chair; in β-glucose, epimeric with mannose at C2, this sequence is equatorial-equatorial-equatorial, and in the tetradentate complexes that β-glucose forms with alkali metal cations, the pyranose ring assumes a boat conformation (Cerda and Wesdemiotis 1999, Botek et al 2001). Likewise, in the α anomeric form of MeMan, the axial hydroxyl O2 allows for tridentate interaction with the pyranose ring oxygen and the hydroxymethyl group.

C. Advantage of DFT Methods over Simulated Annealing for Conformational Analysis of
Sodiated Structures

The simulated annealing molecular dynamics (SAMD) protocol, described in the previous chapter and applied to the neutral α- and β- anomers of methyl-D-manno-pyranoside, was tested on the sodiated structure Na$^+$-αMeMan1. In order to carry out simulated annealing studies of Na$^+$-monosaccharide complexes, the ligand-metal binding interaction must be described within the empirical force field framework. Stote and Karplus (1995) distinguish between "bonded" and "nonbonded" models for describing the binding of a metal to a protein or other biological molecule.

"Bonded" models are those which account for interactions between the metal ion and its ligand atoms by introducing explicit bond and angle terms with associated parameters into the potential energy function, thereby restricting the conformational flexibility of the binding site; "nonbonded" models, on the other hand include only van der Waals and electrostatic terms.

The development of a "bonded" model for Na$^+$-carbohydrate interactions through the determination of equilibrium values for bond lengths and angles was considered beyond the scope of this project. A "nonbonded" method was attempted instead, in which electrostatic charges (q) for Na$^+$ and its O ligands were obtained from Mulliken population analyses, as was done for simulations of neutral structures. The Lennard-Jones (6-12) parameters σ and ε for Na$^+$ (Beglov and Roux 1994), which describe van der Waals interactions, were obtained from the CHARMM22 protein parameter set. The carbohydrate system with the Na$^+$ ion was found to be unstable in the majority of simulations, as the geometries and energy values obtained were extremely unrealistic in most cases.

In their paper on the development of force field parameters for molecular dynamics simulations of zinc-containing proteins, Stote and Karplus (1995) discuss the application of harmonic constraints defined as $k(r - r_o)^2$, where k is the force constant with units of kcal/mol-Å^2, to energy minimization and solution-phase dynamics simulations of two proteins containing bound Zn^{2+}. During the sequence of heating and equilibration steps used in the dynamics simulation, different harmonic constraint force constants were used during different steps.

Given the partially covalent character (10-20%) of the Na^+-O bonds in the Na^+-MeMan adducts as determined by Mayer bond order analysis (vide supra), the use of harmonic distance restraints would be useful in performing simulated-annealing molecular dynamics studies of a monosaccharide-sodium ion adduct. The harmonic character of the distance constraints mimics that of a covalent bond without requiring one to determine equilibrium bond lengths and angles as in a "bonded" model.

Determining the best force constants for harmonic restraints applied during each step in the simulated annealing protocol was considered beyond the scope of this project. In addition, as Na^+ binding reduces the rotational degrees of freedom of the coordinating hydroxyl and methoxyl groups, the number of possible low-energy minima, and thus the need for simulated annealing, decreases. For these reasons, the simulated annealing method was reserved for generating a series of candidate structures for the neutral methyl hexopyranoside anomers. For studies of the sodiated structure, the strategy of Cerda and Wesdemiotis (1999)—generating an ensemble of conformers which were then geometry-optimized and their relative energies compared—was employed instead.

III. Analysis of Experimental Data

Dwivedi and colleagues (2006) calculated collisional cross-sections (Ω) for the α and β complexes from drift times measured in different drift gases. Separation factors (α) between α and β anomeric complexes were also calculated from drift times (t_d). To obtain in vacuo radii for comparison to theoretical results, the collision cross-section data from Table 4.6 were analyzed using the method of zero-polarizability radii described in Chapter 2.

Table 4.6 Drift times (t_d), collisional cross-sections (CCS), and separation factors for [methyl-D-mannopyranoside]Na$^+$ anomers in Ar, N_2, and CO_2.[a]

Drift gas	α		β		Separation factor
	t_d (ms)	CCS (Å^2)	t_d (ms)	CCS (Å^2)	
N_2 [b]	12.79	122	12.61	120	1.01
Ar [c]	18.11	118	17.92	117	1.02
CO_2 [c]	20.96	164	20.42	160	1.03

a) All measurements carried out at a flow rate of 1300 mL/min and a pressure of 700 mmHg.
b) Experiments carried out at 401 V/cm.
c) Experiments carried out at 514 V/cm.

As shown in Table 4.7 and Figure 4.8, the slope of the α-[MeMan]Na$^+$ curve is slightly higher, indicating that the two species can be separated at higher polarizability values. This is consistent with the fact that separation (defined as a difference in drift times greater than 0.2 ms between α and β anomers) is observed only in CO_2—the most polarizable of the three drift gases employed (Table 4.6).

A. Zero-Polarizability Radii

The experimentally determined radii are higher than the theoretical values by a factor of approximately 0.7 Å. This error appears systematic, and is likely to be related to the approximations used for determining the size of the theoretical structures (radius of

gyration) and for determining radius from experimentally determined collisional cross-section (the hard-sphere approximation). The radius of gyration is by definition an underestimate of the molecule's true size, as it does not account for the fact that the drift gas molecules interact not with nuclei but with the electron cloud of the ion. Likewise, the hard-sphere approximation used to calculate ion radius from collisional cross-section overestimates radius because it does not account for medium- and long-range ion-neutral interactions.
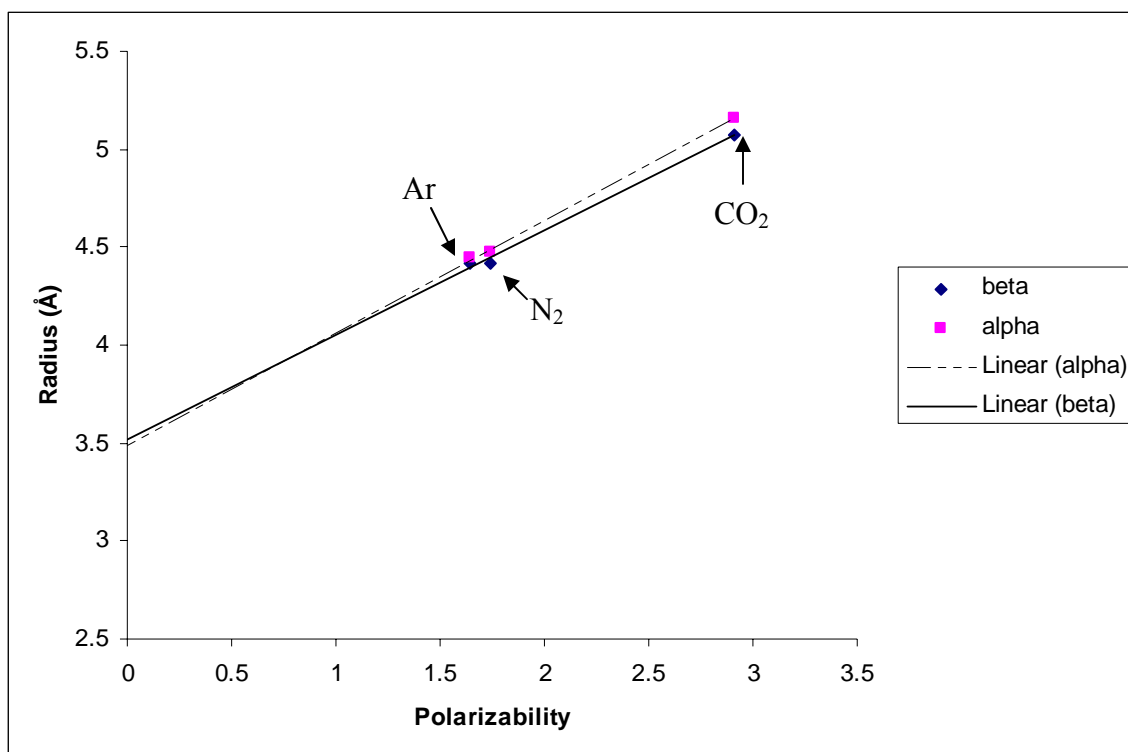
Figure 4.8 Radius vs drift gas polarizability for α- and β-[methyl-D-mannopyranoside]Na$^+$. Drift gases used were Ar (polarizability 1.641×10^{-24} cm^3), N$_2$ (polarizability 1.740×10^{-24} cm^3), and CO$_2$ (polarizability 2.911×10^{-24} cm^3.)

Table 4.7 Regression data for the two curves shown in Fig 4.8.

	Slope	Intercept	R^2
α-[MeMan]Na$^+$	0.575 ± 0.023	3.486 ± 0.049	0.998
β-[MeMan]Na$^+$	0.533 ± 0.038	3.519 ± 0.082	0.995

As seen in Table 4.8, the experimental and theoretical values of the difference in radii (r_β - r_α) are relatively close to one another (0.033 and 0.054 Å, respectively). Both experimental and theoretical (r_β - r_α) values are within the standard deviation of the experimental results, indicating that under zero-polarizability conditions, the size difference between the anomeric adducts is extremely small. In addition, theoretical structures and extrapolation of experimental results to zero polarizability give the same prediction of the relative radii of the two anomeric complexes ($r_\beta > r_\alpha$). Most significantly, the greater radius for the β anomeric form relative to the α anomeric form is inconsistent with the pattern of the experimental drift times and calculated cross-sections, in which the α anomeric form invariably drifts slower and thus shows a greater collisional cross-section than the β anomeric form.

Table 4.8 Comparison of experimental and theoretical radii calculated for α- and β-[methyl-D-mannopyranoside]Na$^+$.

	Ion radius (Å)		(r_β - r_α) (Å)
	α	β	
Experimental	3.486 ± 0.05	3.519 ± 0.08	0.033
Theoretical (R_g)	2.762	2.816	0.054

B. Dipole Moment

The increase in separation factor with drift gas polarizability, along with the discrepancy between the two anomeric species' relative drift times/collision cross sections and relative radii indicates that a hard-sphere collision model that neglects ion-neutral interactions is insufficient to account for the interaction of the two anomeric complexes with the drift gas. Non-centrosymmetric ions such as the anomeric [MeMan]Na$^+$ complexes are likely to have a permanent dipole moment, which is capable

of polarizing the electron distribution of the neutral gas molecule, resulting in an electrostatic interaction (known as a Debye interaction) between the two species.

A model based on permanent-dipole-induced dipole interactions suggests that of two similarly-sized isomers, the species with the higher overall dipole moment would interact more strongly with the drift gas, and thus would have a greater drift time and collisional cross-section. To determine whether this prediction is correct, dipole moments for theoretical structures were calculated in Gaussian 03 (Table 4.9). Surprisingly, the two α-anomeric complexes not only have smaller radii, but also smaller overall dipole moments than the β complex, suggesting that neither size (as predicted by a hard-sphere collision model) nor dipole moment (as predicted by an permanent dipole-induced dipole model) can account for the relative drift times and collision cross-sections of α- and β-[MeMan]Na$^+$.

Table 4.9 Dipole moments (Debye) for α- and β-[methyl-D-mannopyranoside]Na$^+$ calculated at the B3LYP/6-31G* level of theory.

	Components			Overall
	x	y	z	
α (*tg-g+*)	2.423	-1.413	4.089	4.958
α (*ttt*)	-1.664	3.908	3.677	5.618
β	6.102	-2.192	0.898	6.546

The dipole moments of α- and β-[MeMan]Na$^+$ differ significantly in the magnitudes of their x and z components, with both α conformers having dipole moments whose x components are much smaller than their z components. The dipole moment of the β anomeric complex, on the other hand, has an x component larger than the overall dipole moments of the α conformers, and its z component is significantly smaller than those of the α conformers.

It is commonly assumed that ion motion is not aligned by the electric field under "low-field" or thermal conditions (energy acquired by the ion from the electric field is negligible relative to the thermal energy.) Under these conditions the large differences in the x and z components of the anomeric [MeMan]Na$^+$ complexes' dipole moments are expected to be of little relevance, as the ion's rotational motion is essentially random. On the other hand, if the electric field is sufficiently high to allow partial alignment of the ion along **E,** the difference could affect the ions' relative collisional cross-sections.

Aligning the dipole (**p)** is dependent on the work A needed to flip the dipole, relative to the available rotational energy U_R (Shvartsburg et al 2006). For a dipole of moment p set at an angle a relative to the electric field vector **E** the work required to flip the dipole is given by

$$A = \int_0^{\pi} pE \sin a \, da = 2pE \tag{4.1}$$

As there are two rotational axes orthogonal to **p**, each having a mean thermal energy of $kT/2$; the mean rotational energy $\langle U_R \rangle$ is thus equal to kT; the free rotation regime for the ion requires $A << \langle U_R \rangle$.

Calculation of the values of A for dipoles between 5-7 D and electric field values of 401 and 514 V/cm indicate that the energy required to flip the dipoles of α- and β-[MeMan]Na$^+$ is at least three orders of magnitude smaller than the mean rotational energy kT under experimental conditions. This provides a clear indication that the ion is thermalized and rotates randomly, so the differences in the direction of the dipole moment are not relevant to ion-drift gas interactions under experimental conditions.

CHAPTER FIVE

CONCLUSION

Density functional theory calculations indicate that when coordinating the sodium cation, both α- and β-methyl-D-mannopyranoside (MeMan) behaves much like other hexose species such as glucose and galactose, preferring tri- or tetradentate coordination involving the hydroxymethyl group. Lowest-energy structures were identified for the sodium adducts of both anomers, indicating that the axial orientation of the C2 hydroxyl group of MeMan allows it to engage in tri- or tetradentate binding of the Na^+ cation while retaining the stable $^4C_1$ chair conformation of the neutral methyl glycoside.

Stable complexes formed by the two anomers differ in their coordination numbers and in the geometry of their coordination sites. In α-[MeMan]Na^+, the coordination is tridentate, involving the hydroxymethyl oxygen O6, the pyranose ring oxygen O5, and the axial hydroxyl oxygen O2. The coordination site is symmetric, as the bond lengths are roughly equivalent. In β-[MeMan]Na^+, the coordination is tetradentate, as the equatorial orientation of the anomeric oxygen O1 allows it to participate in binding the cation. The coordination site is asymmetric, as the Na^+-O1 bond distance is significantly larger than the other three bond distances. Both complexes were found to be further stabilized by the presence of intramolecular hydrogen bonds between the ring hydroxyl groups, and the conformations of the ring hydroxyl groups of α-[MeMan]Na^+ were determined to interconvert readily at the temperature of the drift tube.

Radii of gyration calculated for the theoretical structures showed them to be of similar size, with β-[MeMan]Na^+ being slightly larger than α-[MeMan]Na^+. The zero-polarizability approximation was used to obtain experimental radii for comparison to the modeled radii from collisional cross sections obtained in different drift gases. While the

experimental radii were significantly larger than modeled radii, experimental and modeled radii agreed well in describing the relative sizes and the difference in radius between the α and β complexes.

The relative sizes (β-[MeMan]Na$^+$ > α-[MeMan]Na$^+$) predicted by the lowest-energy theoretical structures and the application of the zero-polarizability approximation to experimental data were in significant contrast to the experimentally determined drift times and collisional cross-sections. In each drift gas used in the previous experimental studies, α-[MeMan]Na$^+$ has a longer drift time and larger collisional cross-section than β-[MeMan]Na$^+$. In CO_2, these differences are large enough to allow baseline separation of the two anomers as sodium adducts. The discrepancy between relative radii and relative drift times/ collision cross-sections indicates that α-[MeMan]Na$^+$ and β-[MeMan]Na$^+$ are not separated according to size.

As the experimentally observed increase in separation factor with drift-gas polarizability indicated a possible role for ion-induced dipole interactions in determining the drift time and collisional cross-sections of each anomeric complex, dipole moments were calculated for the theoretical structures of α- and β-[MeMan]Na$^+$. While a greater dipole moment might be expected to predict greater interaction between the ion and a polarizable drift gas, and thus an increased drift time and collisional cross-section, overall dipole moment, like size, was found to be greater for β-[MeMan]Na$^+$ than α-[MeMan]Na$^+$. Since neither ion size nor magnitude/direction of ion dipole adequately predict the differential interactions of the two anomeric [MeMan]Na$^+$ complexes with the drift gases, further study, possibly including electrostatic potential mapping of the ions and potential energy surface scans for the ion-neutral pair carried out using large basis sets, is required to determine the mechanism by which these two species are separated.

REFERENCES

Chapter One

ASBURY, G.R. & HILL, H.H., JR. (2000) Using different drift gases to change separation factors (alpha) in ion mobility spectrometry. *Analytical Chemistry*, 73, 3028-34.

BEEGLE, L.W., KANIK, I., MATZ, L. & HILL, H.H., JR. (2002) Effects of drift gas polarizability on glycine peptides in ion mobility spectrometry. *International Journal of Mass Spectrometry*, 216, 257-68.

BEEGLE, L.W., KANIK, I., MATZ, L. & HILL, H.H., JR. (2001) Electrospray ionization high-resolution ion mobility spectrometry for the detection of organic compounds, I. Amino Acids. *Analytical Chemistry*, 73, 3028-34.

BJORNDAL, H., LINDBERG, B. & SVENSSON, S. (1967) Mass spectrometry of partially methylated alditol acetates. *Carbohydrate Research,* 5, 433-40.

COLAS, C., BOUCHONNET, S., ROGALEWICZ-GILARD, F., POPOT, M.-A. & OHANESSIAN, G. (2006) Proton and sodium cation affinities of harpagide: a computational study. *Journal of Physical Chemistry A*, 110, 7503-8.

CECH, N.B. & ENKE, C.G. (2001) Practical implications of some recent studies in electrospray ionization fundamentals. *Mass Spectrometry Reviews*, 20, 362-87.

CLOWERS, B.H., DWIVEDI, P., STEINER, W.E., HILL, H.H., JR. & BENDIAK, B. (2005) Separation of sodiated isobaric disaccharides and trisaccharides using electrospray ionization atmospheric pressure ion mobility time of flight mass spectrometry. *Journal of the American Society for Mass Spectrometry*, 16, 660-69.

DELL, A. & MORRIS, H.R. (2001) Glycoprotein structure determination by mass spectrometry. *Science*, 291, 2351-6.

DRICKAMER, K. & TAYLOR, M.E. (2006) *Introduction to Glycobiology,* 2nd ed. London: Oxford University Press.

DUUS, J.O., GOTTFREDSEN, C.H. & BOCK, K (2000) Carbohydrate structure determination by NMR spectroscopy: modern methods and limitations. *Chemical Reviews,* 100, 4589-4614.

DWIVEDI, P., BENDIAK, B., CLOWERS, B.H. & HILL, H.H., JR. (2006) Rapid resolution of carbohydrate isomers by electrospray ionization ambient pressure ion mobility spectrometry/time-of-flight mass spectrometry (ESI-APIMS-TOFMS). *Journal of the American Society for Mass Spectrometry*, in press.

GABRYELSKI, W. & FROESE, K.L. (2003a) Rapid and sensitive differentiation of anomers, linkage, and position isomers of disaccharides using high-field asymmetric

waveform ion mobility Spectrometry (FAIMS). *Journal of the American Society for Mass Spectrometry*, 14, 265-77.

GABRYELSKI, W. & FROESE, K.L. (2003b) Characterization of napthenic acids by electrospray ionization high-field asymmetric waveform ion mobility Spectrometry. *Analytical Chemistry*, 75, 4612-23.

HAGEN, D.F. (1979) Characterization of isomeric compounds by gas and plasma chromatography. *Analytical Chemistry*, 51, 870-4.

HONDA, S. (1996) Separation of neutral carbohydrates by capillary electrophoresis. *Journal of Chromatography A,* 720, 337-51.

HILL, H.H., JR., HILL, C.H., ASBURY, G.R., WU, C., MATZ, L.M. & ICHIYE, T. (2002) Charge location on gas-phase peptides. *International Journal of Mass Spectrometry*, 219, 23-37.

IMANARI, T., TOIDA, T., KOSHIISHI, I. & TOYODA, H. (1996) High-performance liquid chromatographic analysis of glycosaminoglycan-derived oligosaccharides. *Journal of Chromatography A*, 720, 275-93.

KARASEK, F.W. & KANE, D.M. (1974) Plasma chromatography of isomeric halogenated nitrobenzenes. *Analytical Chemistry* 46, 780-2.

LEAVELL, M.D, GAUCHER, S.P., LEARY, J.A., TARASZKA, J.A., CLEMMER, D.E. (2002) Conformational studies of Zn-ligand-hexose diastereomers using ion mobility measurements and density functional theory calculations. *Journal of the American Society of Mass Spectrometry*, 13, 284-94.

LEE, D.S., WU, C. & HILL, H.H., JR. (1998) Detection of carbohydrates by electrospray ionization ion mobility spectrometry following microbore high-performance liquid chromatography. *Journal of Chromatography A*, 822, 1-9.

LEE, S., WYTTENBACH, T. & BOWERS, M.T. (1997). Gas-phase structures of sodiated oligosaccharides by ion mobility/ion chromatography methods. *International Journal of Mass Spectrometry and Ion Processes*, 167, 605-14.

LIU, Y. & CLEMMER, D.E. (1997) Characterizing oligosaccharides using injected-ion mobility mass Spectrometry. *Analytical Chemistry*, 69, 2504-9.

MATZ, L.M., HILL, H.H., JR., BEEGLE, L.W. & KANIK, I. (2002) Investigation of drift gas selectivity in high-resolution ion mobility spectrometry with mass spectrometry detection. *J Am Soc Mass Spectrometry*13, 300-7.

WU, C., SIEMS, W.F., KLASMEIER, J. & HILL, H.H., JR. (2000) Separation of isomeric peptides using electrospray ionization/high resolution ion mobility spectrometry. *Analytical Chemistry,* 72, 391-5.

ZAIA, J. (2002) Mass spectrometry of oligosaccharides. *Mass Spectrometry Reviews*, 23, 161-227.

Chapter Two

ASBURY, G.R. & HILL, H.H (2000) Evaluation of ultrahigh resolution ion mobility spectrometry as an analytical separation device in chromatographic terms. *Journal of Microcolumn Separations,* 12, 172-8.

REVERCOMB, H.E. & MASON, E.A. (1975) Theory of plasma chromatography. *Analytical Chemistry*, 47, 970.

SIEMS, W.F., WU, C., TARVER, E.E., HILL, H.H., JR., LARSEN, P.R. & MCMINN, D.G. (1994) Measuring the resolving power of ion mobility spectrometers. *Analytical Chemistry*, 66, 4195-4201.

STEINER, W.E., CLOWERS, B.H., FÜHRER, K., GONIN, M., MATZ, L.M., SIEMS, W.F., SCHULTZ, A.J. & HILL, H.H., JR. (2001) Electrospray ionization with ambient pressure ion mobility separation and mass analysis by orthogonal time-of-flight mass spectrometry. *Rapid Communications in Mass Spectrometry*, 15, 2221-6.

WU, C., SIEMS, W.F., ASBURY, G.R. & HILL, H.H., JR. (1998) Electrospray ionization high-resolution ion mobility spectrometry- mass spectrometry. *Analytical Chemistry* 70, 10.

Chapter Three

BECKE, A.D. (1993). A new mixing of Hartree-Fock and local density-functional theories. *Journal of Chemical Physics*, 98, 1372.

BOCK, K. & PEDERSEN, C. (1983) Carbon-13 nuclear magnetic resonance spectroscopy of monosaccharides. *Advances in Carbohydrate Chemistry and Biochemistry*, 41, 27-66.

BROOKS, B.R., BRUCCOLERI, R.E., OLAFSON, B.D., STATES, D.J., SWAMINATHAN, S. & KARPLUS, M. (1983) CHARMM: a program for macromolecular energy, minimization, and dynamics calculations. *Journal of Computational Chemistry*, 4, 187-217.

CERDA, B. & WESDEMIOTIS, C. (1999) Thermochemistry and structures of Na^+-coordinated mono- and disaccharide stereoisomers. *International Journal of Mass Spectrometry*, 189, 189-204.
DOWD, M.K. FRENCH, A.D. & REILLY, P.J. (1994) Modeling of aldopyranosyl ring puckering with MM3 (92). *Carbohydrate Research*, 264, 1-19.

FRISCH, M.J., TRUCKS, G.W., SCHLEGEL, H.B., SCUSERIA, G.E., ROBB, M.A., CHEESEMAN, J.R., MONTGOMERY, J.A., JR., VREVEN, T., KUDIN, K.N., BURANT, J.C., MILLAM, J.M., IYENGAR, S.S., TOMASI, J., BARONE, V.,

MENNUCCI, B., COSSI, M., SCALMANI, G., REGA, N., PETERSSON, G.A, NAKATSUJI, H., HADA, M., EHARA, M.,TOYOTA, K., FUKUDA, R., HASEGAWA, J., ISHIDA, M., NAKAJIMA, T., HONDA, Y., KITAO, O., NAKAI, H., KLENE, M., LI, X. KNOX, J.E., HRATCHIAN, H.P., CROSS, J.B., BAKKEN, V., ADAMO, C., JARAMILLO, J., GOMPERTS, R., STRATMANN, R.E., YAZYEV, O., AUSTIN, A.J., CAMMI, R., POMELLI, C., OCHTERSKI, J.W., AYALA, P.Y., MOROKUMA, K., VOTH, G.A., SALVADOR, P., DANNENBERG, J.J., ZAKRZEWSKI, V.G., DAPPRICH, S., DANIELS, A.D., STRAIN, M.C., FARKAS, O., MALICK, D.K., RABUCK, A.D., RAGHAVACHARI, K., FORESMAN, J.B., ORTIZ, J.V., CUI, Q., BABOUL, A.G., CLIFFORD, S., CIOSLOWSKI, J., STEFANOV, B.B., LIU, G., LIASHENKO, A., PISKORZ, P., KOMAROMI, I., MARTIN, R.L. , FOX, D.J., KEITH, T., AL-LAHAM, M.A., PENG, C.Y., NANAYAKKARA, A., CHALLACOMBE, M., GILL, P.M.W., JOHNSON, B., CHEN, W., WONG, M.W., GONZALEZ, C., POPLE, J.A. (2003). *Gaussian 03*, revision B.05; Pittsburgh, PA: Gaussian, Inc.

GONZALEZ, L., MO, O. & YAÑEZ, M. (1997) High-level *ab initio* calculations on the intramolecular hydrogen bond in thiomalonaldehyde. *Journal of Physical Chemistry A*, 101, 9710-19.

HA, S.N., GIAMMONA, A., FIELD, M. & BRADY, J.W. (1998) A revised potential-energy surface for molecular mechanics studies of carbohydrates. *Carbohydrate Research*, 180, 207-21.

HOCKNEY, R.W. (1970). The potential calculation and some applications. *Methods in Computational Physics*, 9, 136-211.

HOHENBERG, P. & KOHN, W. (1964) Inhomogeneous electron gas. *Physical Review*, 136, B864.

HOYAU, S. & OHANESSIAN, G. (1997) Complexation of small organic molecules by Cu^+. *Chemical Physics Letters*, 280, 266-72.

KIRKPATRICK, S., GELATT, C.D., JR. & VECCHI, M.P. (1983) Optimization by simulated annealing. *Science*, 220, 671.

KOHN, W. & L.J. SHAM. (1965) Self-consistent equations including exchange and correlation effects. *Physical Review*, 140, A1133.

LEE, C., YANG, W. & PARR, R.G. (1985) Development of the Colle-Salvetti correction energy formula into a functional of the electron density. *Physical Review B*, 37, 785.

MACKERELL, A.D., JR., BROOKS, B., BROOKS, C.L., III, NILSSON, L. ROUX, B., WON, Y., KARPLUS, M. (1998). CHARMM: The Energy Function and Its Parameterization with an Overview of the Program, in *The Encyclopedia of Computational Chemistry*, 1, 271-277, SCHLEYER, P.V.R., *et al.*, editors. Chichester: John Wiley & Sons.

QUINTON, J. (2006). In press.

RAO, V.S.R, QASBA, P.K., BALAJI, P.V. & CHANDRASEKARAN, R. (1988) *Conformation of Carbohydrates*. London: Taylor & Francis, 1998.

SCHLEGEL, H.B. (1982). Optimization of equilibrium geometries and transition structures**.** *Journal of Computational Chemistry*, 3, 214.

SHALLENBERGER, R.S. (1982) *Advanced Sugar Chemistry*. Westport, CT: AVI Publishing.

VIJAYALAKSHMI, K.S., YATHINDRA, N. & RAO, V.S.R. (1973). Theoretical studies on the conformations of methyl glycosides. *Carbohydrate Research*, 31, 173-81.

VOSKO, S.H., WILK, L. & NUSAIR, M. (1980) Accurate spin-dependent electron liquid correlation energies for local spin density calculations: a critical analysis. *Canadian Journal of Physics,* 58, 1200.

Chapter Four

BRIDGEMAN, A.J. & CAVIGLIASSO, G. (2003) Towards an understanding of the bonding in polyoxometalates through bond order and bond energy analysis. *Faraday Discussions*, 124, 239-258.

BRADY, J.W. & SCHMIDT, R.K. (1993) The role of hydrogen bonding in carbohydrates: molecular dynamics simulations of maltose in aqueous solution. *Journal of Physical Chemistry, 97*, 958-66

BOTEK, E., DEBRUN, J.L., HAKIM, B. & MORIN-ALLORY, L. (2001) Attachment of alkali cations on beta-D-glucopyranose: matrix-assisted laser desorption/ionization time-of-flight studies and ab initio calculations. *Rapid Communications in Mass Spectrometry*, 15, 273-6.

CRAMER, C.J. & TRUHLAR, D.G. (1993) Quantum chemical conformational analysis of glucose in aqueous solution. *Journal of the American Chemical Society,* 115, 5745-53.

GUO, B.C., CONKLIN, B.J. & CASTLEMAN, A.W., JR. (1989) Thermochemical properties of ion complexes $Na^+(M)_n$ in the gas phase. *Journal of the American Chemical Society*, 111, 6506-10.

HORI, H.Y., NISHIDA, Y., OHRUI, H., MEGURO, H. (1990) Conformational analysis of hydroxymethyl group of D-mannose derivatives using (6S)(6-H-2)-D-mannose and (6R)-(6-H-2)-D-mannose. *Journal of Carbohydrate Chemistry*, 9, 601-618.

MARCHESSAULT, R.H. & PEREZ, S. (1979) Conformations of the hydroxymethyl group in crystalline aldohexopyranoses. *Biopolymers*, 18, 2369-74.

MAYER, I. (1984) Charge, bond order and valence in the AB initio SCF theory. *Chemical Physics Letters*, 97, 270-4.

NISHIDA, Y., HORI, H., OHRUI, H. & MEGURO, H. (1988) ^{1}H NMR analyses of rotameric distribution of C5-C6 bonds of D-glucopyranoses in solution. *Journal of Carbohydrate Chemistry*, 7, 239-50.

PENG, C. & SCHLEGEL, H.B. (1993) Combining synchronous transit and quasi-Newton methods to find transition states. *Israel Journal of Chemistry*, 33, 449.

SHVARTSBURG, A.A., BRYSKIEWICZ, T., PURVES, R.W., TANG, K., GUEVREMONT, R. & SMITH, R.D. (2006) Field asymmetric waveform ion mobility spectrometry studies of proteins: dipole alignment in ion mobility spectrometry? *Journal of Physical Chemistry B*, 110, 21966-80.

STEINER, T. (2002) The hydrogen bond in the solid state. *Angewandte Chemie International Edition*, 41, 48-76.

STEINER, T. & SAENGER, W. (1992) Geometric analysis of non-ionic O-H---O hydrogen bonds and non-bonding arrangements in neutron diffraction studies of carbohydrates. *Acta Crystallographica*, B48, 818-27.

STOTE, R.H., & KARPLUS, M. (1995) Zinc binding in proteins and solution: a simple but accurate nonbonded representation. *Proteins: Structure Function and Genetics*, 23, 12-31.

SUNDARALINGAM, M. (1968) Some aspects of stereochemistry and hydrogen bonding of carbohydrates related to polysaccharide conformations. *Biopolymers*, 6, 189-213.

ZHENG, Y.J., ORNSTEIN, R.L. & LEARY, J.A. (1997) A density functional theory investigation of metal ion binding sites in monosaccharides. *Journal of Molecular Structure (THEOCHEM),* 15, 273-9.